Brodogradnja Volume 77 Number 4 (2026) 77413

University of Zagreb Faculty of Mechanical Engineering and Naval Architecture

journal homepage: www.brodogradnja.fsb.hr

Brodogradnja

An International Journal of Naval Architecture and Ocean Engineering for Research and Development

Micro-ROV tethered to HOV for deep-sea observation: design, implementation and experimental validation

Jinrong Zheng[1,2], *Xianbo Xiang*[1,3,4], *Shaolong Yang*[1,3,4], *Jialei Zhang*[1,3,4,*], *Baosheng Li*[2], *Jing Leng*[2]

[1] *School of Naval Architecture and Ocean Engineering, Huazhong University of Science and Technology, Hubei 430074, China*
[2] *Department of Deep-Sea Technology and Engineering, Institute of Deep-Sea Science and Engineering, Chinese Academy of Sciences, 28 Luhuitou Road, Sanya 572000, China*
[3] *International Science and Technology Cooperation Offshore Center for Ship and Marine Intelligent Equipment and Technology, Hubei, China*
[4] *Wuhan Belt & Road Joint Lab of Ship and Marine Intelligent Equipment and Technology, Hubei, China*

ARTICLE INFO

Keywords:
Human occupied vehicle (HOV)
Remotely operated vehicle (ROV)
Lightweight design
Deployment and recovery device
Deep-sea trials

ABSTRACT

Human-occupied vehicles (HOVs), constrained by substantial volume and weight, encounter significant challenges in exploring complex seabed terrains, such as rugged seabed and confined operational spaces. To compensate for the limitations of HOV, a micro-observation-class remotely operated vehicle (ROV) tethered to the HOV Shen Hai Yong Shi was developed to enhance HOV's exploration capability in complex seabed terrains. This paper, for the first time, presents an overall design of the functions and composition of the deep-sea micro-observation-class ROV system. In the design of the micro ROV mechanical, electrical and control systems, the payload space, weight and energy constraints of the HOV are considered. A power supply and communication scheme is designed for the ROV from the mother HOV via an optoelectronic composite umbilical cable. This scheme provides sufficient weight margins and spatial allocation for the thrusters and detection sensors, thereby significantly optimising the ROV's performance in terms of lightweighting and motion maneuverability. The design concept of the micro-observation-class ROV, mounted on the HOV Shen Hai Yong Shi, has been comprehensively validated during a sea trial at a depth of 1,380 m.

1. Introduction

Deep-sea exploration constitutes a critical technology for the development of marine resources, the study of Earth's evolutionary processes and the protection of marine ecosystems [1-3]. Deep-sea technology has undergone a paradigm shift from mechanical sampling to intelligent autonomous detection [4-6]. A deep-sea vehicle serves as a versatile platform that can carry various sonar equipment, mechanical sampling devices, scientific research instruments and scientists to deep-sea environments rapidly and accurately for precise exploration and investigation [7]. The human-occupied vehicle (HOV) is a class of deep-sea vehicle that has attracted significant attention worldwide due to its technological advantages in in situ observation and

* Corresponding author.
E-mail address: jlzhang009@hust.edu.cn

https://doi.org/10.21278/brod77413
Received 27 September 2025; Received in revised form 05 July 2026; Accepted 10 July 2026
Available online 29 July 2026
ISSN 0007-215X; eISSN 1845-5859

underwater manipulation [8]. China's independently developed manned submersibles, Shen Hai Yong Shi and Fen Dou Zhe, have achieved remarkable success in the field of deep-sea exploration [9].

Nonetheless, the volume and weight constraints limit HOVs' performance in high-precision detection and intervention tasks in complex seabed terrains, such as rugged bathymetry and confined operational spaces. To compensate for these limitations, a mother–child underwater robotic system has been developed, in which a micro-observation-class remotely operated vehicle (ROV) is deployed from an HOV for enhanced exploration capability [10]. On 1 September 1985, the HOV Alvin carried the ROV Jason Junior for close-up observations of the Titanic wreck lying on the Atlantic seabed [11]. This ROV, approximately 0.71 m long, was equipped with a high-resolution camera and an illumination system. In September 2001, two deep-sea micro-observation-class ROVs were deployed from the HOVs Mir I and Mir II to conduct a week-long detailed survey of the Titanic wreck at a depth of 3,700 m [11, 12], with Jake and Elwood ROVs, respectively, that operated in conjunction with their host submersibles, demonstrating a remarkable deep-sea exploration mission. In 2014, the ROV Long Zhu, developed by the Shenyang Institute of Automation, Chinese Academy of Sciences, was successfully deployed from the HOV Jiao Long [13, 14]. It recorded the near-seabed high-resolution observations of the Caiwei Seamounts in the northwestern Pacific at a depth of 2,424 m, capturing the first deep-sea image of the HOV Jiao Long. Further improvements in the integration of such deep-sea observation ROVs are feasible as science and technology advance rapidly. In addition, enhancing the overall system performance within volume and weight constraints will effectively support deep-sea detection and intervention tasks.

The high hydrostatic pressure in the deep sea imposes stringent requirements on the pressure tolerance and sealing performance of deep-sea equipment. In addition, the extreme deep-sea environment is characterised by low temperature, darkness, corrosion and complex ocean currents, which further exacerbate the operational difficulties and uncertainties of such equipment [5, 15, 16]. The development of a deep-sea micro-observation-class ROV system is a systematic engineering endeavor [17]. Typically, ROV consists of a primary frame, buoyancy modules, camera and lighting units, a control unit, a monitoring system and a propulsion system [18-20]. Each subsystem must undergo precise design to ensure that the overall ROV fulfills its intended functions [21]. Motion control is critical to the underwater dynamic observation performance of ROVs. The motion control of underwater vehicles is characterised by model inaccuracies, high nonlinearity and strong coupling effects [22], compounded by unpredictable current disturbances from the surrounding environment. Consequently, the motion control system of an ROV must simultaneously exhibit superior maneuverability, stability and robustness [23]. The commonly studied and applied algorithms for underwater vehicle motion control include proportional-integral-derivative (PID) control [24], sliding mode control [25], model predictive control [26] and the rapidly evolving intelligent control methods [27]. Among these, PID is the most classical control algorithm in control theory and has been extensively adopted in engineering practice [28, 29]. Based on the above considerations, this paper designs and develops a micro-observation-class ROV system.

2. General design

Investigations show that deep-sea observation ROVs tethered to an HOV carry their own battery, which is used to power their peripheral devices, limiting the maximum subsea operating time of the ROV to 3 hours. Compared with land-based operations, the underwater operating environment is complex and often accompanied by unpredictable situations, thus requiring sufficient operating time to ensure the smooth progress and completeness of underwater inspection. The micro-observation ROV based on the HOV Shen Hai Yong Shi introduced in this paper is powered by an external power supply. It is connected to the HOV Shen Hai Yong Shi via an optoelectronic composite umbilical cable and is powered by the HOV's batteries. Since the HOV has ample power supply, the underwater operating time of the ROV is nearly unrestricted. Without the need for a battery, thus the ROV itself can accommodate more thrusters. An increase in the number of actuators significantly improves the ROV's maneuvering performance, making underwater operations more efficient. In addition, cameras with better imaging quality can be selected to obtain high-resolution real-time video, further enhancing the ROV's underwater operational capability. As shown in Table

1, both ROV xBot III from Phoenix Company and ROV Long Zhu are equipped with a battery and low-resolution cameras. The deep-sea observation ROV studied in this paper adopts an external power supply mode, is equipped with 6 thrusters and a 4K camera, and demonstrates superior performance to the former two.

Table 1 Comparison of Parameters of Deep-Sea Micro-Observation-Class ROVs

Index	xBot III [30][32]	Long Zhu	Studied by this paper
Dimensions (cm)	56×33×35	40×36×38	46×40×37.5
Weight (kg)	50	38.5	39.08
Depth (m)	6000	7000	6000
Working time (h)	3	3	/
Thrusters Qty.	3	3	6
Cameras	PAL CAM×2	PAL CAM×1	4K CAM×1 PAL CAM×1
Illustration		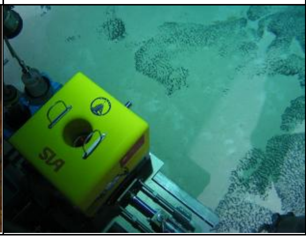	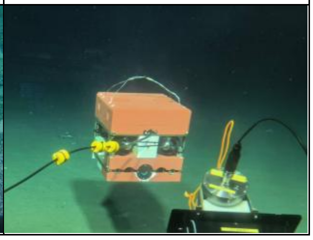

In addition to the ROV itself, the deep-sea micro-observation system tethered to the HOV Shen Hai Yong Shi also includes a launch and recovery system and a remote monitoring system. The ROV and the launch and recovery system are installed above the sampling basket of the HOV, while the remote monitoring system is deployed inside the manned spherical cabin. The ROV is connected to the HOV via an umbilical cable through the launch and recovery system, enabling power and signal transmission. The pilot inside the manned spherical cabin monitors and controls the status of the ROV and the launch and recovery system through the remote monitoring system. The 3D layout diagram and the physical illustration of the deep-sea micro-observation system are shown in Figure 1.

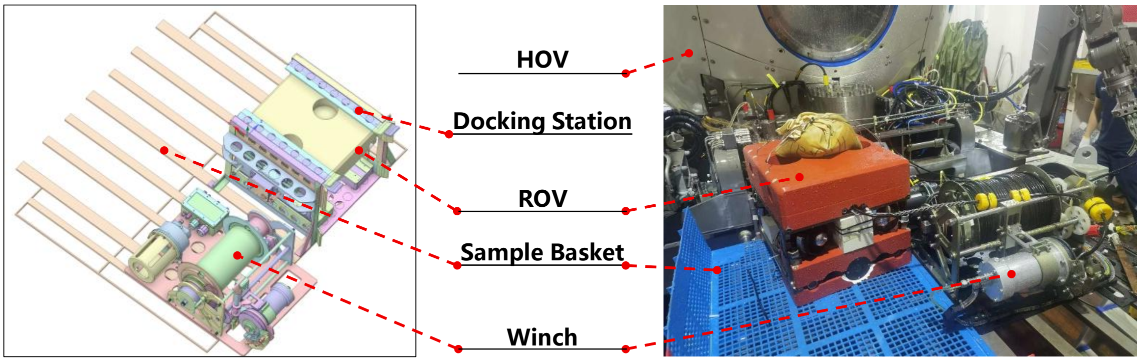

Fig. 1 3D Layout diagram and physical illustration of the deep-sea micro-observation-class ROV system

Once the HOV Shen Hai Yong Shi reaches the working area, the pilot operates the docking device on the docking station to release the ROV, allowing it to be free. Subsequently, the ROV is maneuvered to exit the docking station. When the ROV is flying far away from the HOV, the pilot simultaneously operates the traction winch to pay out the umbilical cable. Upon arriving at the desired exploration area, the ROV takes a close look at the target area using its multiple onboard lights and cameras. After completing the observations, the pilot operates the ROV to fly back to the docking station while concurrently operating the main winch to recover the umbilical cable. Finally, the ROV is secured by the docking station's locking mechanism. The launch and recovery system consists of a docking station and a winch unit. The docking station is used to accommodate, lock, and release the ROV. The winch unit primarily comprises a cable reel, main motor, optoelectronic slip ring, transmission components, cable laying device, traction motor, tensioning assembly, and so on. The physical illustration of the winch unit is presented in Figure 2.

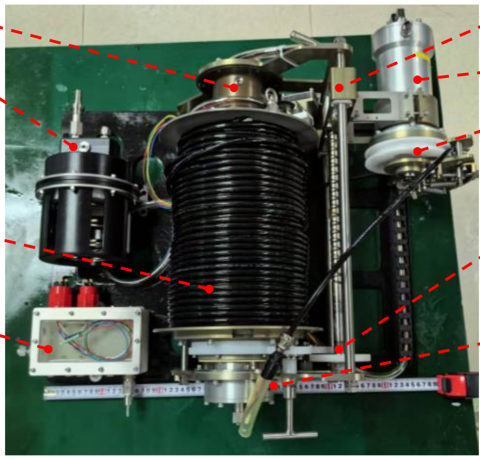

Fig. 2 Physical illustration of the deployment and recovery winch

Parameters of the deployment and recovery device are shown in Table 2.

Table 2 Parameters of the deployment and recovery device

Index	Parameter
Weight of winch (kg)	25
Cable reel diameter (mm)	160
Cable reel width (mm)	305
Cable Length (m)	>60
Maximum recovery speed (m/s)	0.077
Maximum release speed (m/s)	0.103
Maximum pulling tension (kg)	28.5
Dock station internal dimensions (mm)	425×460×450
Weight of dock station (kg)	7

The remote monitoring system is connected to the remotely operated vehicle (ROV) via a fiber optic link, enabling the acquisition of real-time status updates and the remote control of ROV movements. Additionally, the system interfaces with the controller of the deployment and recovery device through a serial communication interface to operate the winch unit and docking mechanism remotely. The remote monitoring system comprises components for power conversion, photoelectric conversion, signal interconnection, computer control, as well as video display and storage functionalities. The HOV supplies 24 V DC to the hardware, with the input power being converted to isolated 24 V DC and 12 V DC to power equipment such as the computer, switch, optoelectronic conversion module, serial server, and video capture card. Pilots utilize two joysticks to operate the winch and ROV independently. Two external monitors are connected to the control box to display the human-machine interface (HMI) and video feeds from both cameras.

The computer within the control box operates the monitoring system software, which is developed on the Windows operating system. This software utilizes a vector-based rendering engine from the Windows Presentation Foundation framework to leverage modern graphics hardware and is structured around the Model-View-ViewModel (MVVM) architectural pattern. The MVVM pattern distinctly separates the application's business logic from its user interface, ensuring that the view remains entirely independent of the application logic. The system comprises four Human-Machine Interface (HMI) pages: the main page, the power management page, the motion control page, and the database management page. The main page's content is organized into nine distinct regions, as illustrated in Figure 3.

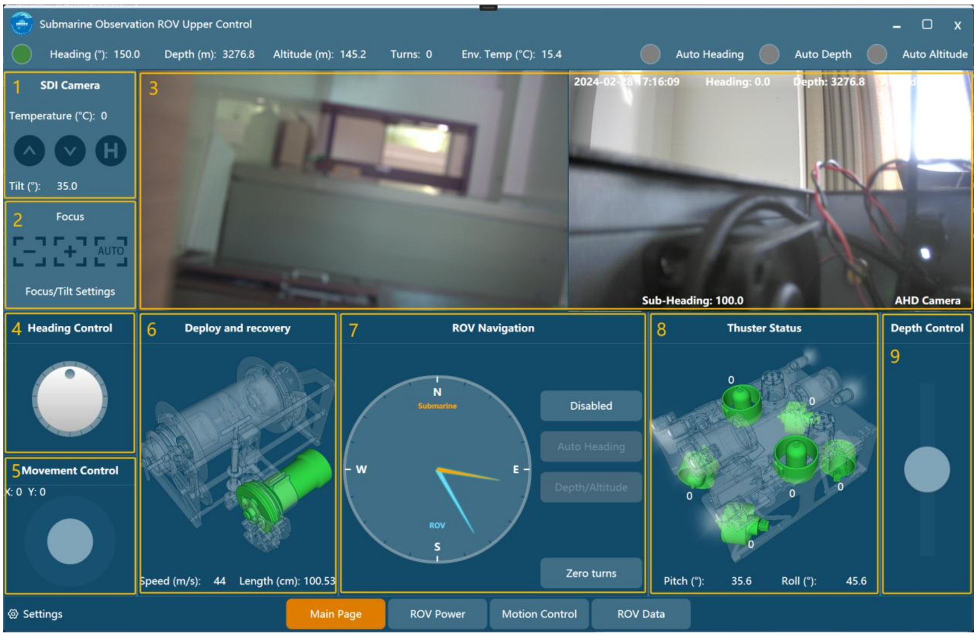

Fig. 3 Main page of HMI

Each dive of a HOV may involve multiple operational tasks. In addition to installing the ROV system, the sampling basket must also be capable of carrying other experimental devices or operational tools. Consequently, the ROV system can only occupy a limited amount of space above the sampling basket, and there are specific weight limitations for the ROV system. The external power supply mode can significantly extend the operational time of the ROV. However, the battery from the HOV has a power limitation, with a maximum output capacity of 110 V/10 A. Therefore, when designing the ROV power system and motion control algorithms, it is essential to consider the limitations of the input power.

3. Mechanical system

3.1 Composition

The deep-sea micro-observation-class ROV developed in this study weighs 39.08 kg in air, with dimensions of 460 mm in length, 400 mm in width, and 375 mm in height. The ROV is equipped with six electrically driven thrusters. Two vertically mounted thrusters are dedicated to heave control. The remaining four thrusters are arranged in a horizontal over-actuated configuration, allowing omnidirectional motion in the horizontal plane as well as yaw rotation. This propulsion layout also provides a degree of fault tolerance and enhances the vehicle's operational reliability especially in horizontal surface. Additionally, the ROV features automatic motion control functions, such as auto-heading and auto-altitude. It is configured with a fiber-optic transmission 4K camera, enabling real-time transmission of high-resolution video images. This ROV has no limitation on working time subsea as long as the HOV has sufficient power.

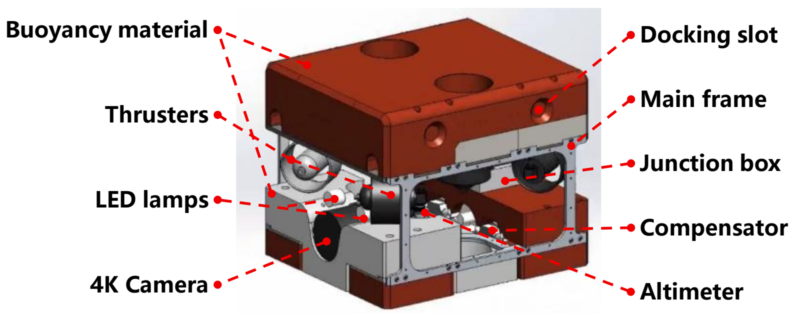

Fig. 4 3D Model of the micro-observation ROV

The ROV comprises a main frame, buoyancy material, a junction box, peripheral equipment, and waterproof cables. Figure 4 shows the 3D model of the complete ROV. Four thrusters are arranged in a vectored configuration in the horizontal plane, and two thrusters are installed in the vertical plane. A 4K-resolution camera is deployed at the forward end of the ROV with four LED lamps, and a PAL camera is deployed at the stern with two LED lamps. An altimeter is mounted on the underside of the ROV. At the centre of the ROV, there is a junction box, which provides interfaces for peripheral devices such as thrusters, cameras, LED lamps, altimeters, and compensators. The junction box also provides an interface for the umbilical cable to transmit power and fibre-optic signals. A series of circuit boards are installed inside the junction box to perform power distribution, data acquisition, and thruster control, while also integrating other basic sensing capabilities onboard. All peripheral equipment and buoyancy materials are mounted on the main frame, which is fabricated from 7075 aluminium alloy. The surface of the main frame is treated with anodising for corrosion protection. To further enhance corrosion resistance, zinc blocks are installed on the aluminium alloy frame as sacrificial anodes. The parameters of ROV peripherals are shown in Table 3.

Table 3 Parameters of ROV Peripherals

Item	Quantity	Parameter
Thruster	6	W100-48-4500-AL-BL 48 V/PWM/500 W/5 kg
lamp	6	LED/White/12 V/18 W
Forward camera	1	4K/SDI/Auto focus/12 V
Backward camera	1	1080P/AHD/12 V
Compensator	2	130 ml/alarm
Altimeter	1	ISA500/50 m/12 V/RS232

3.2 Design concepts

Once all the parameters of peripheral devices decided, which including 3D models of all peripherals, weights in air and water, we can start overall design of the ROV. In the process of developing the whole structure of the ROV, the following design principles are followed:

(1) Clarify the size and weight boundaries of the entire ROV. The overall length, width, and height dimensions of the machine should be reasonably allocated, and the appearance is compact and coordinated.

(2) The ROV should have slight positive buoyancy when completely submerged subsea, while positive buoyancy less than 0.5 kg.

(3) The ROV should maintain a stable attitude subsea without obvious inclination under nature condition.

(4) It is necessary that the centre of buoyancy is higher than the center of gravity, and there is no need to excessively pursue the height difference between the center of buoyancy and the centre of gravity.

(5) Thrust action line of four horizontal thrusters should be as close as possible to the same horizontal plane as the center of gravity of the ROV.

(6) The structural strength of the main frame should be sufficient, and all peripherals and cables should be layout reasonably, friendly to disassembly, assembly, and maintenance.

The high pressure at a depth of 6000 m poses significant technical challenges for the high flexibility and small-sized design of neutral buoyancy optoelectronic composite umbilical cable. Engineers finally selected a low-cost solution, which is a normal waterproof cable has an outer diameter of approximately 8 mm and weighs about 20 g/m subsea. Since the ROV does not have the capability to adjust its pitch and roll angle actively, engineers installed multiple small floating balls on the umbilical cable close to the ROV end to balance the weight of the cable weight under water, thus reducing the impact of the umbilical cable weight on ROV motion control.

3.3 Key parameters

The density of buoyancy material selected for the deep-sea micro-observation-class ROV is 0.58. To limit weight of the whole ROV, it is important to reduce the weight of the ROV main frame and accessories as much as possible, thereby reducing the weight of buoyancy material required for trimming buoyancy and further reducing the total weight of ROV.

Due to its small size, the deep-sea observation ROV is very sensitive to weight. During the design processing, it is essential to accurately count the weight and volume of each peripheral device, cable, connector, etc., to ensure that the selected buoyancy material is appropriate and meets the expected requirements. The statistical results of the air mass, volume, subsea mass, and buoyancy of all ROV components are shown in Table 4.

Table 4 Statistics data of ROV Mass and Buoyancy

Parameters	Weight in air (kg)	Volume (l)	Buoyancy (kg)	Weight in water (kg)
Main frame	3.26	1.16	1.19	2.07
Junction box	4.25	3.06	3.15	1.10
Thrusters	6.30	1.56	1.61	4.69
4K camera	2.18	0.64	0.66	1.52
PAL camera	1.28	0.55	0.57	0.71
LED lamps	0.77	0.17	0.18	0.59
Altimeter	0.50	0.15	0.15	0.35
Compensators	1.24	0.77	0.79	0.45
Cable	0.94	0.71	0.73	0.21
Above total	20.72	8.77	9.03	11.69
Buoyancy material	17.33	30.40	31.31	-13.98
Total	38.05	39.17	40.35	-2.30

When calculating buoyancy based on component volumes, the gravitational acceleration g is taken as 9.8 m/s², and the seawater density is 1.03 g/cm³. Theoretical calculations show that the ROV has a mass of 38.05 kg in air, a volume of 39.17 l, and a total buoyancy of approximately -2.30 kg. The actual mass of the ROV is 39.08 kg with an underwater buoyancy of 0.45 kg, matching the expected design requirements. According to statistical and computational analysis, the difference of 1.85 kg between calculated buoyancy and measured buoyancy is mainly attributed to incomplete component statistics and inaccurate parameter statistics such as component size and density in Table 4. On the one hand, Table 4 only accounts for major components with large mass and volume, while numerous small items on the ROV were not included. These include bolts, spring washers, flat washers, O-rings, and the control circuit boards housed within the junction box. Notably, some bolts used to secure the buoyancy modules to the main frame are relatively long and contribute non-negligible mass. In addition, the subsea cable employed is not a conventional rubber pressure-resistant cable, but a custom oil-filled cable. In Table 4, only the weights of the hose and white mineral oil were roughly estimated. The mass of the internal conductors within the oil-filled cable and the 316L stainless steel end connectors were not considered. Furthermore, the cable length was estimated rather than precisely measured, introducing additional uncertainty. On the other hand, two different approaches were used to estimate component weights. Some components (e.g., thrusters and cameras) were measured directly by weighing them both in air and underwater. Others (e.g., the main frame and buoyancy materials) were evaluated using a three-dimensional model. Inevitably, discrepancies exist between the numerical model and the physical components, including differences between the assigned material densities in the software and the actual material properties, as well as geometric deviations between the modeled and fabricated parts.

Given the density difference between seawater and freshwater is 0.03 g/cm³ and ignoring the compression effect of deep-sea pressure on the ROV, the buoyancy difference of the ROV between freshwater and seawater is 1.18 kg. To satisfy both pool testing and marine test conditions, an interface in the center area of the ROV is designed for installing counterweights. During pool testing, counterweights of appropriate weight are removed to ensure the ROV is in a state of slight positive buoyancy, facilitating ROV testing in the pool. The center of gravity (CG) and center of buoyancy (CB) can be calculated using 3D modeling software. With the geometric center of the ROV main frame defined as the coordinate origin, the CG is located at (10.93, 1.57, −6.10 mm), whereas the center of the horizontal thruster array is located at (9.99, 0.00, −0.50 mm). This indicates that the thrust line of the horizontal propulsion system is approximately aligned with the CG and lies nearly in the same horizontal plane. The CB is located at (10.25, 0.28, 12.21 mm), corresponding to a vertical separation of 18.31 mm above the CG, which satisfies the established static stability design requirements.

3.4 Hydrodynamic drag analysis

To satisfy the design requirement that the ROV be capable of maintaining operation against currents of up to 2 knots, thrusters with adequate thrust output must be selected. In this study, computational fluid dynamics (CFD) is employed to numerically investigate the hydrodynamic drag acting on the ROV at different operating speeds, thereby providing a basis for thruster selection. The detailed simulation procedure is described as follows:

(1) Geometric simplification: Small geometric features, such as holes, grooves, minor chamfers, and fillets, which have negligible influence on the overall flow field but may lead to mesh distortion and excessive mesh density, are removed. Internal cavities are treated as solid regions. The simplified geometric model of the ROV is shown in Figure 5(b).

(2) Computational domain setup: Owing to the geometric symmetry of the ROV, only one-half of the vehicle model, separated by the longitudinal symmetry plane, is considered in the simulation to improve computational efficiency. Let the overall length, width, and height of the ROV be denoted by L, W, and H, respectively. The distances from the ROV to the inlet and outlet boundaries of the computational domain are set to 5L and 10L, respectively. The distances to the upper and lower boundaries are both 3H, while the distance to the lateral boundary is 3 W. The resulting computational domain is illustrated in Figure 5(c).

(3) Mesh generation: The fluid domain is imported into ANSYS Fluent for mesh generation. For the surface mesh, the minimum element size is 7.1875 mm, the maximum element size is 100 mm, and the growth rate is set to 1.2. Polyhedral cells are employed for volume meshing, with a maximum cell size of 126.5 mm. The generated surface and volume meshes are shown in Figure 5(d) and Figure 5(e), respectively.

(4) Solver configuration: Following mesh quality verification, the numerical solver is configured in ANSYS Fluent. The inlet velocity is specified as 1.0289 m/s. The lateral, upper, and lower boundaries are defined as moving walls with a translational velocity of 1.0289 m/s. The k–ω SST turbulence model is adopted together with a pressure–velocity coupling scheme. Convergence is considered achieved when the residuals of continuity, the three velocity components, turbulent kinetic energy (k), and specific dissipation rate (ω) are all reduced below 0.001.

(5) Numerical computation and post-processing: The flow field is initialized prior to the formal simulation. Upon convergence, the hydrodynamic drag acting on the ROV is extracted, and the surface pressure distribution and flow streamlines are obtained through post-processing.

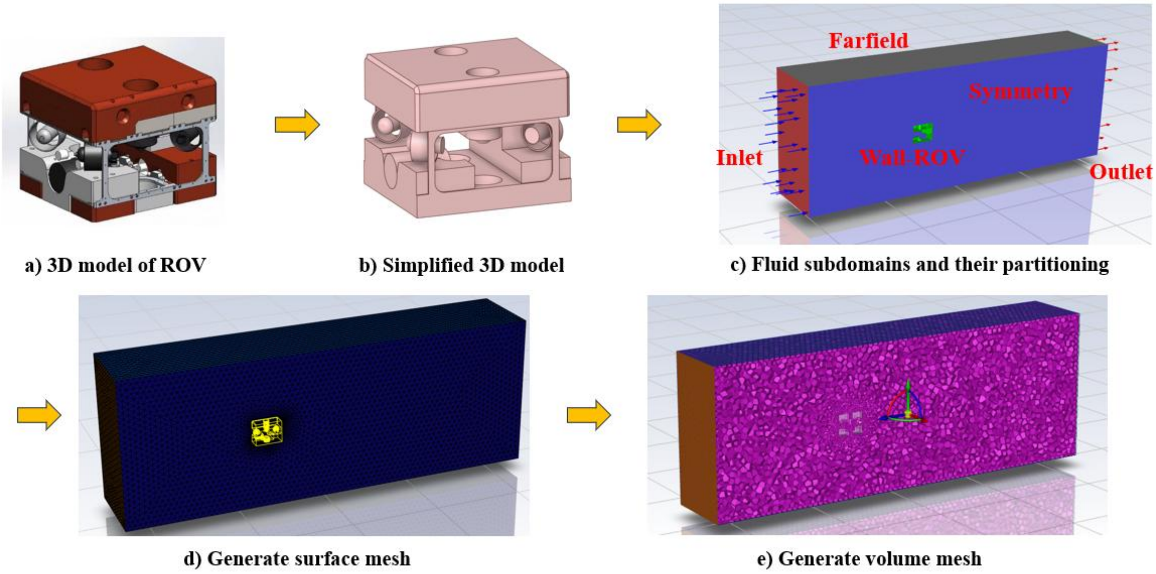

Fig. 5 CFD simulation pre-processing procedure

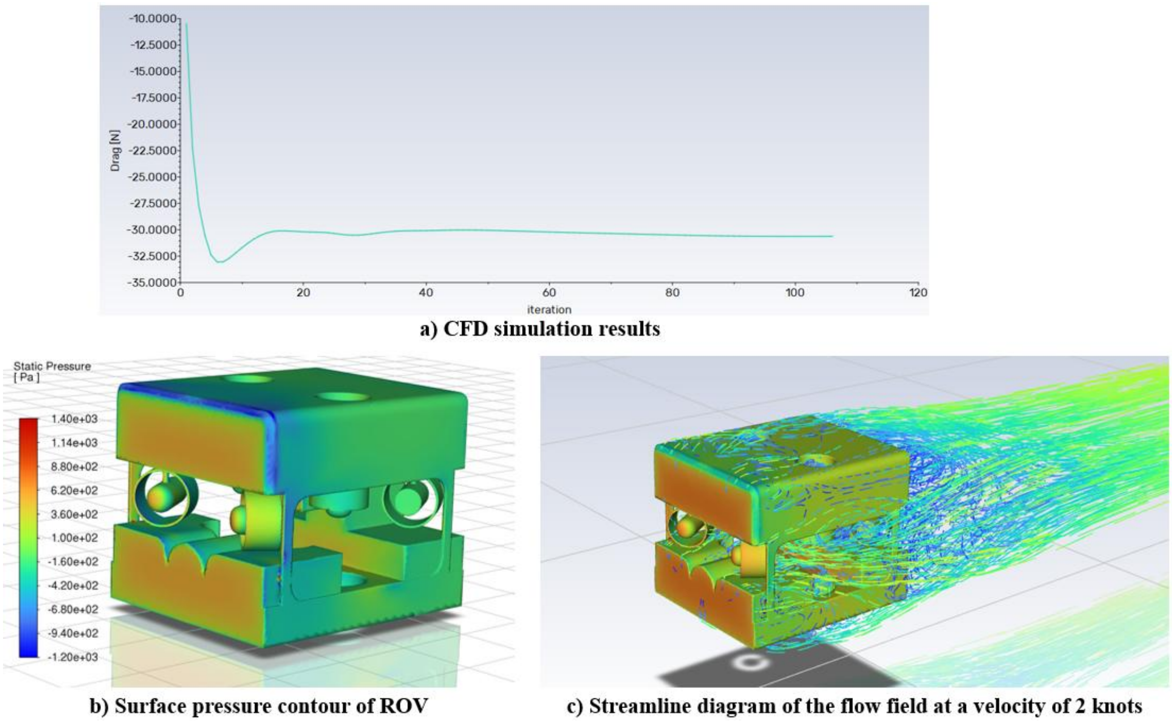

Fig. 6 CFD simulation results and post-processing data

The numerical simulation reached convergence after 106 iterations. The results indicate that, at a forward speed of 2 knots, the hydrodynamic drag acting on the half-model in the direction of motion is 30.63 N, corresponding to a total drag force of 61.26 N for the full-scale model. Figure 6 illustrates the surface pressure distribution and flow streamlines around the ROV at a speed of 2 knots. The streamline pattern and pressure distribution reveal the formation of a high-pressure stagnation region at the bow, which constitutes the primary source of hydrodynamic resistance. Within the frame structure, the flow is significantly disturbed by the vertical members and onboard components, resulting in complex local vortex structures and increased viscous dissipation. Flow separation occurs in the stern region, leading to the formation of a low-velocity wake characterized by a substantial pressure deficit, which further contributes to pressure drag. Overall, the internal flow disturbances associated with the open-frame configuration and the flow separation occurring at the stern are identified as the dominant contributors to the hydrodynamic resistance of the ROV.

3.5 Umbilical cable disturbance analysis

While the use of a photoelectric composite umbilical cable for remote power transmission significantly enhances the operational endurance of the ROV, the potential adverse effects of a large-diameter umbilical on the motion dynamics of an inherently power-limited vehicle remain a critical issue. Therefore, a quantitative evaluation of the influence of the umbilical cable on ROV maneuvering performance is essential for overall system design.

As shown in Figure 7, during straight-line forward motion of the ROV, the suspended umbilical cable connected to the aft section exhibits a typical catenary configuration under the coupled effects of submerged self-weight (wet weight) and uniform ocean current. Cable self-weight induces vertical tension, whereas cross-flow ocean currents generate horizontal hydrodynamic drag acting normal to the cable axis. These two types of distributed loading act simultaneously on the ROV stern, introducing additional horizontal and vertical disturbance forces. Such cable-induced disturbances degrade the vehicle's attitude stability, increase the load demand on both horizontal and vertical thrusters, and further reduce the overall dynamic stability of the underwater vehicle.

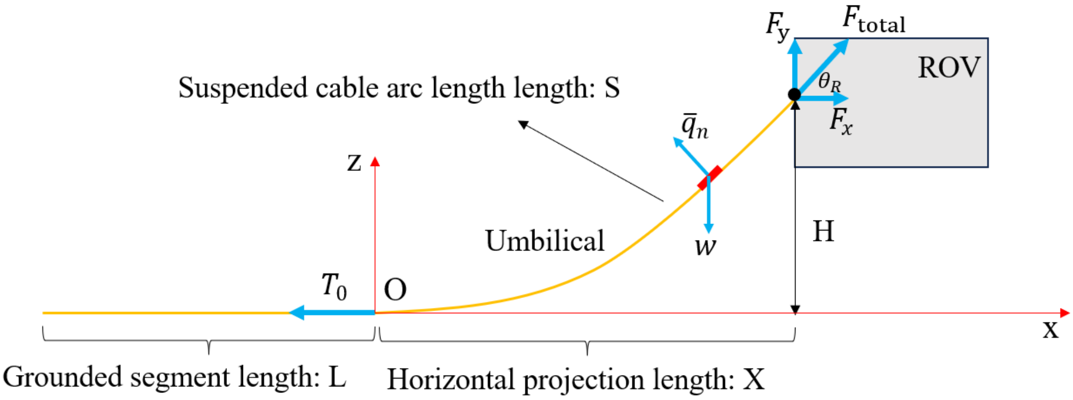

Fig. 7 Force analysis of ROV umbilical cable

To avoid solving the highly nonlinear partial differential equations associated with classical continuous catenary theory, a simplified two-node lumped-mass approach is adopted to model the mechanical behavior of the suspended umbilical cable. In this formulation, the flexible cable is idealized as an equivalent massless rigid segment. The total submerged weight of the cable and the distributed hydrodynamic drag along its length are concentrated at the ROV attachment node. The seabed touchdown point of the cable is treated as another fixed node providing constant horizontal pretension. Based on static force equilibrium, the catenary geometric parameters, distributed hydrodynamic loads, and terminal disturbance forces acting on the ROV are subsequently determined. This simplified approach achieves a balance between computational efficiency and modeling accuracy, making it well suited for the mechanical analysis of umbilical cables under low-speed towing or maneuvering conditions.

The catenary characteristic parameter $a = \frac{T_0}{w}$ is introduced to represent the intrinsic mechanical property of the umbilical cable, where T_0 denotes the horizontal tension at the seabed touchdown point, and w is the submerged (wet) weight per unit length of the underwater cable. Combined with the vertical operating height H of the ROV, the key geometric parameters, including the horizontal projected length, total suspended arc length, and baseline inclination angle, are determined using standard catenary formulations, as given below.

Vertical equilibrium equation of the catenary:

$$\cosh\frac{X}{a} = 1 + \frac{H}{a} \tag{1}$$

Total arc length of suspended cable:

$$S = a \cdot \sinh \frac{X}{a} \tag{2}$$

Baseline inclination angle at ROV terminal:

$$\tan \theta_{base} = \sinh \frac{X}{a} \tag{3}$$

where X is horizontal projection length of the umbilical cable. S is total arc length of the suspended cable segment. θ_{base} is baseline inclination angle at the ROV cable connection end, which is obtained without considering ocean current drag and only considering cable wet weight.

Ocean current flowing perpendicular to the cable axis induces continuous distributed normal hydrodynamic drag along the entire length of the umbilical cable. To simplify the nonlinear hydrodynamic analysis for spatially varying inclination angles, the average inclination angle of the entire cable segment is used to approximate the instantaneous angle variation along the cable. The average inclination angle is determined as follows:

$$\bar{\theta} = \frac{0 + \theta_{base}}{2} \tag{4}$$

The Morison equation is adopted to evaluate the distributed normal hydrodynamic drag per unit length acting on the cylindrical umbilical cable.

$$\bar{q}_n = \frac{1}{2} \rho C_n d U^2 sin^2 \bar{\theta} \tag{5}$$

The total normal hydrodynamic drag acting on the entire suspended cable is obtained by multiplying the unit-length drag by the total suspended arc length of the cable.

$$D = \bar{q}_n \cdot S \tag{6}$$

where ρ is seawater density. C_n is normal drag coefficient of cylindrical cable. d is outer diameter of umbilical cable. U is relative flow velocity between ocean current and ROV.

The total submerged cable weight and the total normal current-induced drag are both lumped at the ROV termination node. Based on this assumption, two-dimensional static equilibrium equations are established to determine the horizontal and vertical disturbance forces exerted by the umbilical cable on the ROV.

$$F_x = T_0 + D \tag{7}$$

Vertical disturbance force (total submerged weight of the suspended cable; for simplicity, the vertical component of hydrodynamic drag is neglected):

$$F_z = w \cdot S \tag{8}$$

The resultant disturbance force and the actual cable inclination angle, accounting for hydrodynamic effects, are expressed as follows:

$$F_{total} = \sqrt{F_x^2 + F_z^2} F_z = w \cdot S \tag{9}$$

$$\theta_R = \arctan\left(\frac{F_z}{F_x}\right) \tag{10}$$

Table 5 Basic Calculation Parameters

Parameter	Symbol	Value	Unit
Catenary characteristic length	a	2	m
Wet weight per unit cable length	w	0.2	N/m
Vertical operating depth of ROV	H	1	m
Seawater density	ρ	1030	kg/m
Normal drag coefficient	C_n	1.2	-
Outer diameter of umbilical cable	d	0.008	m

Relative ocean current velocity	U	1.0289	m/s

According to the calculation procedure described above, the results are summarized as follows:

(1) Horizontal tension at the seabed touchdown point:

$$T_0 = a \cdot w = 2 \times 0.2 = 0.4 \text{ N} \quad (11)$$

(2) Horizontal projected length of the umbilical cable:

$$X = a \cdot \cosh^{-1}\left(1 + \frac{H}{a}\right) = 2 \times \cosh^{-1}(1.5) = 1.9428 \text{ m} \quad (12)$$

(3) Total suspended length of the umbilical cable:

$$S = a \cdot \sqrt{(\frac{H}{a} + 1)^2 - 1} = 2.2361 \text{ m} \quad (13)$$

(4) Seabed tangent angle and mean cable inclination angle:

$$\theta_{base} = 48.19° \quad (14)$$

$$\bar{\theta} = 24.10° \quad (15)$$

(5) Normal hydrodynamic drag per unit cable length:

$$\bar{q}_n = 0.8464 \text{ N/m} \quad (16)$$

(6) Total hydrodynamic drag acting on the suspended section of the umbilical cable:

$$D = \bar{q}_n \cdot S = 1.8972 \text{ N} \quad (17)$$

(7) Vertical disturbance force induced by the submerged weight of the cable:

$$F_z = w \cdot S = 0.4472 \text{ N} \quad (18)$$

(8) Total horizontal disturbance force:

$$F_x = T_0 + D = 2.2927 \text{ N} \quad (19)$$

(9) Resultant disturbance force acting on the ROV:

$$F_{total} = \sqrt{2.2927^2 + 0.4472^2} = 2.336 \text{ N} \quad (20)$$

(10) Actual cable inclination angle considering the effect of current-induced drag:

$$\theta_R = \arctan\left(\frac{0.4472}{2.2927}\right) = 10.99° \quad (21)$$

According to numerical results, the hydrodynamic drag exerted on the umbilical cable is negligible even when the ROV is operating at a forward speed of 2 knots. Under the considered operating conditions, the horizontal disturbance force transmitted through the umbilical cable is considerably larger than the vertical disturbance force. The hydrodynamic loading induced by cross-flow ocean currents dominates the additional end load imposed on the vehicle. The presence of ocean currents significantly increases the horizontal cable tension and substantially decreases the terminal inclination angle, resulting in a noticeable deviation from the cable's static catenary profile.

4. Electrical and control system design

4.1 System architecture

As shown in Figure 8, the electrical and control system of the whole micro-observation ROV system consists of three parts: the ROV part, the launch and recovery device, and the remote monitoring system. The manned submersible supplies two channels of DC power (110 V AC and 24 V DC) and provides two types of signals (optical fiber and serial port), which are respectively connected to the junction box of the launch and recovery device.

The 110 V power wiring and optical fiber are integrated in the junction box and then connected to the input end of the optoelectronic slip ring. The optoelectronic composite umbilical cable connects the output end of the slip ring and links to the ROV junction box, providing power for the ROV and establishing optical fiber communication. At the HOV end, the optical fiber is connected to the remote monitoring system inside the HOV, where a wavelength division multiplexer separates the video data from the communication data. These data are processed by the SDI optical transceiver and serial optical transceiver, respectively, before being transmitted to the main control computer, which displays the HMI. The pilot inside the cabin can remotely control the ROV by operating the main control computer and joysticks. The 24 V power and serial port signal are connected to the junction box of the deployment and recovery device to power all the peripheral devices in the deployment and recovery device. The status of the deployment and recovery device is acquired through the main control board inside the junction box, and the deployment and recovery device is remotely controlled via the remote monitoring system.

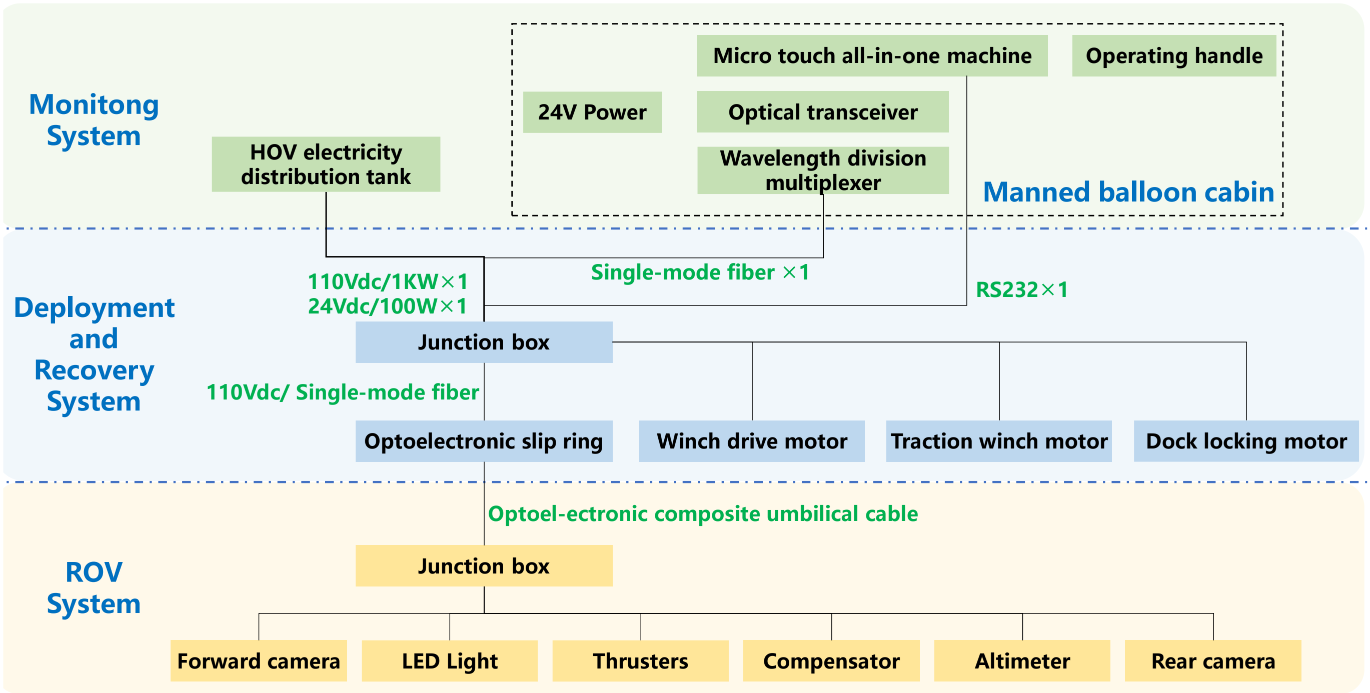

Fig. 8 Electrical and control system of the whole Submersible Observation-Class ROV System

The junction box of the ROV is the electrical and control core of the ROV. As shown in Figure 9, the diagram illustrates the connection between the junction box and peripheral devices. All peripheral devices are centered around the junction box, and all circuit boards are mounted inside the junction box. The control board inside the junction box achieves functions such as power distribution, communication, onboard sensing, camera and lamp control, thruster control, motion control, and interaction with the remote monitoring system. Cables of peripheral devices such as thrusters, cameras, LED lamps, and altimeter are connected to the main control board through the interface of the junction box.

To reduce the overall weight of the ROV, the power conversion boards and main control circuit boards are designed to withstand deep-sea pressure. Inside the junction box, there are four power conversion boards, one main control board, two lamp driver boards, six thruster driver boards, one interface board, and so on. Currently, some electronic components, mainly optical communication modules including coarse wavelength division multiplexers and optical transceivers, cannot directly withstand deep-sea pressure. Therefore, these optoelectronic components are installed in a pressure chamber. To reduce overall weight, the above components are installed inside the backward camera, which not only serves as a camera but also has the function of photoelectric conversion. All cables of the ROV are oil-filled PU tubes. The junction box is connected to all peripheral devices of the ROV through oil-filled tubes. The compensation status can be sensed at any time by reading the value of the level alarm sensor inside the compensator.

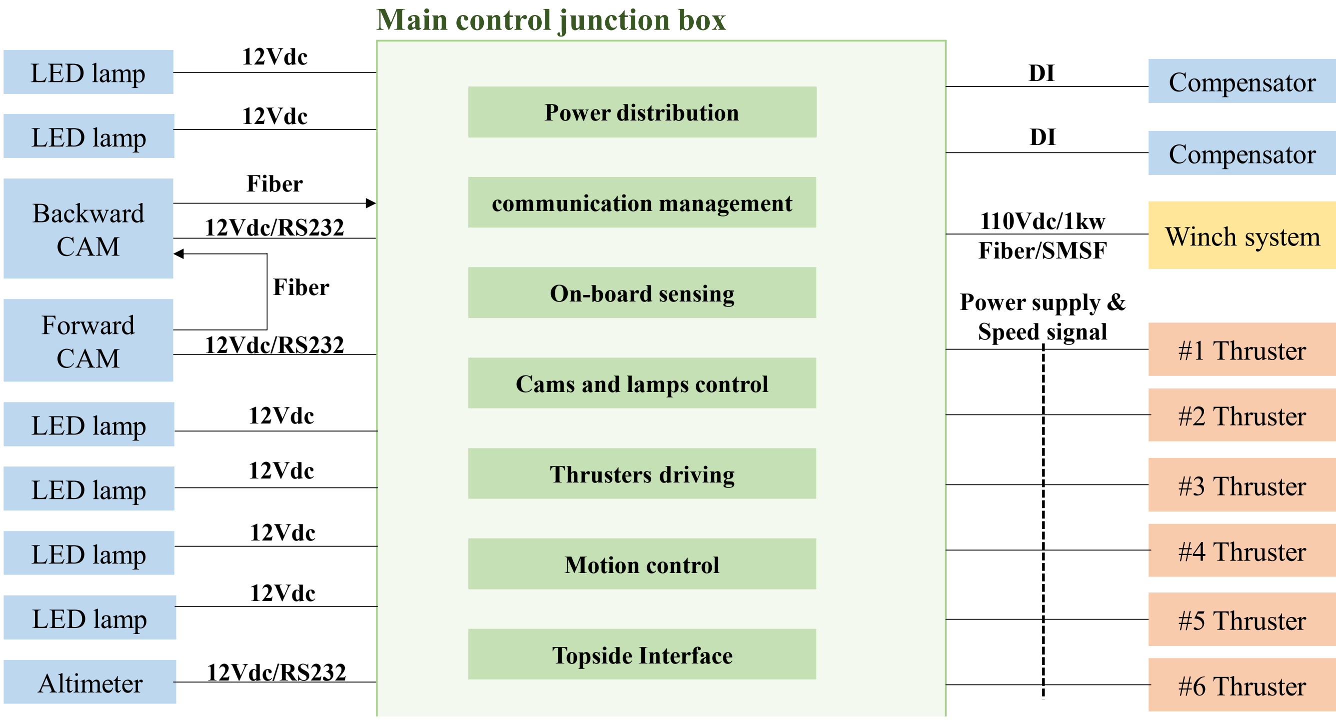

Fig. 9 Connection Diagram of Peripheral Devices with the Main Control Junction Box

4.2 Power supply design

The input voltage of ROV peripheral devices is either 48 V DC or 12 V DC, which are supplied to thrusters and other devices (including LED lamps, cameras, and altimeter). Input power from the manned submersible is 110 Vdc, and DC-DC conversion is completed through the power conversion board to produce two voltage levels: 48 V and 12 V. The power conversion board has an isolation function, which isolates the 110 V from the submersible from the power supply for the ROV electrical system, preventing the submersible's battery from being affected when there is an electrical problem at the ROV end. The 48 V and 12 V power supplies are supplied to various peripheral devices through an optocoupler chip.

To ensure that the power supply from the submersible end matches the power demand of the ROV, it is necessary to calculate the power consumption of the umbilical and ROV. Although the HOV battery pack can provide a maximum output power of 1.1 kW, the design specification limits the power available to the ROV subsystem to 1.0 kW. Accordingly, a battery output power of 1.0 kW is assumed for the power-matching analysis. The umbilical cable between the ROV and the battery is 60 m in length and there are 6 conductors in the umbilical cable, each with a resistance of 40.1 Ω per km. Therefore, the total resistance of the cable is calculated as 1.604 Ω. Considering the submersible battery outputs 1 kW power, the electric current through the umbilical cable under full load is 9.09 A. Therefore, the voltage drop of the umbilical cable can be calculated as 14.58 V, and the power consumption of the umbilical cable is 132.5 W. The input voltage of the ROV power supply is 95.42 V, and the actual maximum available power for the ROV is 867.5 W.

The ROV has 4 power conversion boards, 3 of which are installed with DC-DC modules, converting 110 V to 48 V. Their output ends are connected in parallel to supply power to the thrusters. The other board converts 110 V to 48 V first and then converts 48 V to 12 V through a filtering module. The 12 V is supplied to LED lamps, cameras, altimeter, and control circuit boards. The conversion efficiency of the DC-DC module is greater than 90 % when the input voltage is 95 V at 25 °C, and the efficiency of the filtering module can reach more than 95 % at 25 °C.

Considering the power consumption of peripheral devices, first consider the low-voltage equipment, i.e., equipment other than thrusters, including lights, cameras, altimeter, and control circuit boards. Among these, the power consumption of each LED lamp is 18 W; 6 LED lamps add up to 108 W; two cameras consume 20 W; the altimeter consumes 5 W; the control circuit board consumes about 25 W. The total power consumption is 158 W. The maximum output power of the filtering module is 216 W, which meets the power demand of the low-voltage devices. The working efficiency of the filtering module is 95 %; low-voltage devices consume 185 W at the DC-DC input end at most.

Based on the foregoing calculations, the power available at the thruster input terminals is 682.5 W. Considering the efficiency of the DC–DC conversion stage, the available output power is 614.25 W, assuming a conversion efficiency of 90 %. According to the hydrodynamic simulation results presented in Section 3.4 and the umbilical-induced disturbance analysis in Section 3.5, the ROV must generate approximately 6.48 kgf of forward thrust (equivalent to 63.5 N, with ($g = 9.8\ m/s^2$) to achieve the required cruising speed of 2 knots. Based on the geometric configuration and thrust allocation of the propulsion system, the required thrust produced by each horizontal thruster is approximately 1.98 kgf. Referring to the thruster thrust–power characteristic curve, each horizontal thruster requires an input power of approximately 130 W under this operating condition. Consequently, the total power consumption of the four horizontal thrusters is about 520 W, leaving 94.25 W available for the vertical thruster. Since vertical maneuvers, including ascent and descent, are typically performed at relatively low speeds, the remaining power is sufficient to satisfy the corresponding thrust requirements. In normal operation, the ROV predominantly operates at moderate cruising speeds rather than at maximum propulsion demand. Therefore, the available power of 614.25 W is adequate to meet the vehicle's propulsion and maneuvering requirements. Based on the above analysis and calculations, the onboard battery system is capable of satisfying the overall power demands of the ROV.

4.3 Monitoring function

Figure 10 shows the block diagram of the ROV main control board. The main control board design is based on the STM32F427, which has on-board seawater leakage detection, temperature sensing, and electrical parameter measurement functions. The board acquires seawater leakage status and the temperature of the power board to confirm the control system is safe. By using the PWM output function and pulse input capture function of the MCU, the board connects to six thruster driver boards to control the speed of each thruster and simultaneously gets speed feedback. The MCU controls the power-on and power-off of peripherals through IO ports and achieves auto-focus control of the camera lens and dimming control of the LED lamps via serial ports. The main control board also communicates with the altimeter to obtain the ROV's altitude above the seabed and communicates with the remote monitoring system via RS232 to upload status information of the ROV and receive control commands to complete relevant actions.

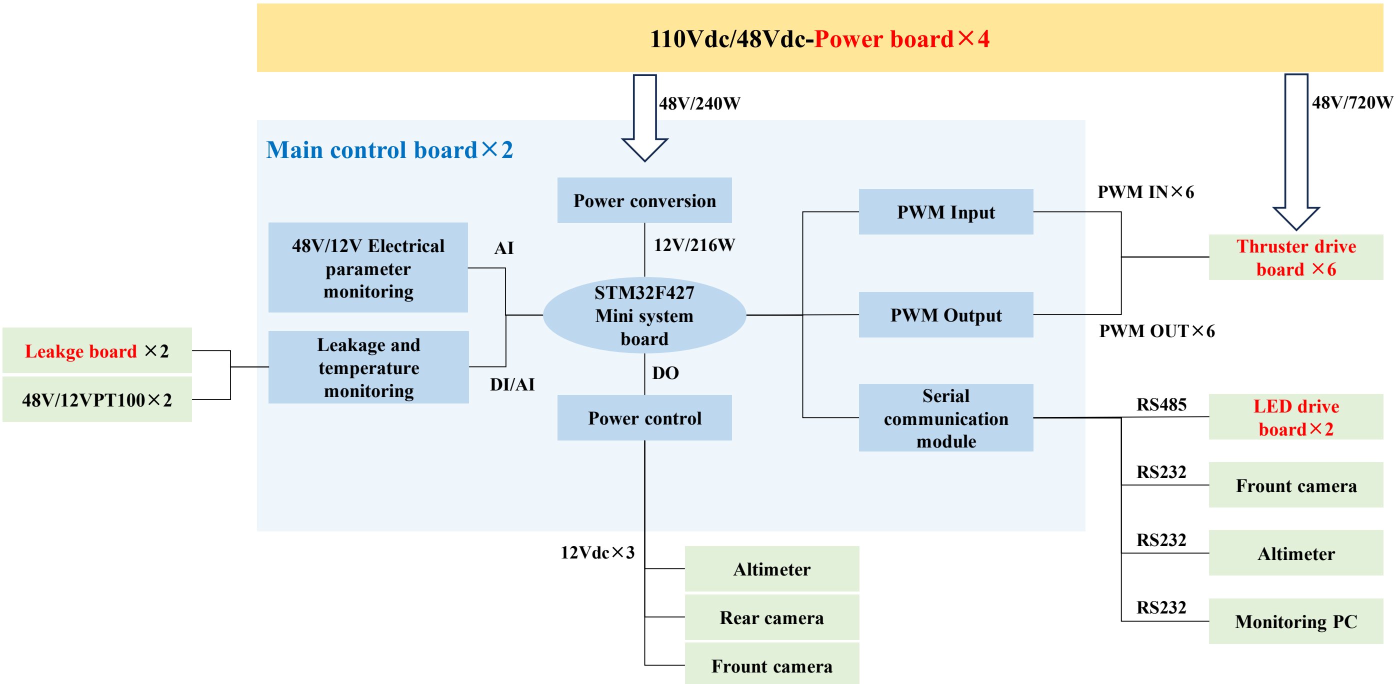

Fig. 10 Block Diagram of ROV Main Control Board

The block diagram of ROV communication is shown in Figure 11. The optical fiber of the umbilical cable is connected to the ROV and split into three wavelengths through a coarse wavelength division multiplexing (CWDM) module. One wavelength (1510 nm) is connected to the SDI optical transceiver for transmitting video data of the SDI camera; the other two wavelengths (1310 nm / 1490 nm) are connected to the AHD optical transceiver. The AHD optical transceiver converts the signal in the optical fiber to one channel of AHD video interface and two channels of RS232 interfaces. The AHD video interface is used to transmit the video data of the PAL camera. One of the RS232 interfaces is connected to the main control board to achieve data communication between the remote monitoring system and the ROV main control board; the other RS232 interface is directly connected to the 4K camera for online adjustment of camera parameters.

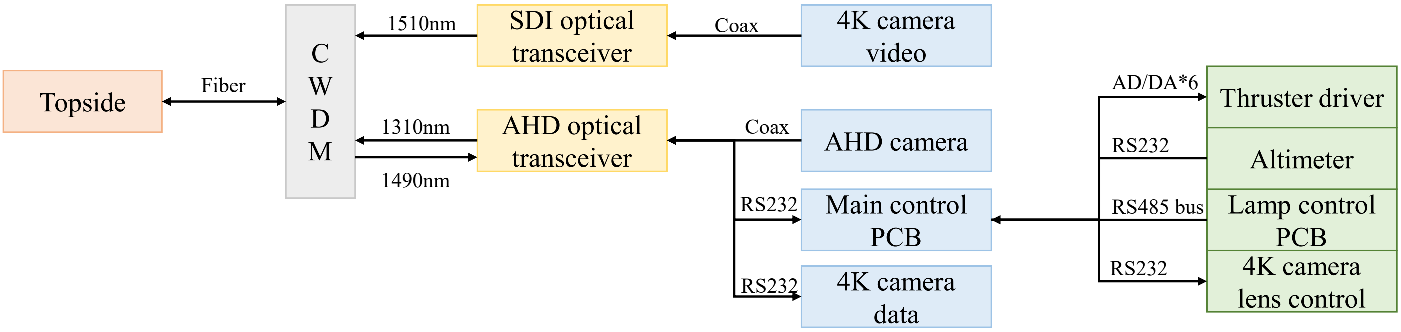

Fig. 11 Block Diagram of ROV Communication

5. Motion control

5.1 Algorithm design

Compared to land vehicles, motion of underwater vehicles is affected by viscous resistance, added mass effects (inertial forces generated by the acceleration of surrounding water), eddy current interference, etc., resulting in a strong nonlinearity in their dynamic models [31]. It is very difficult to establish math model of underwater vehicle accurately and PID algorithm was selected for deep-sea micro-observation ROV motion control, which does not require accurate dynamic model of the robot. PID algorithm has a simple structure, and it is very easy to achieve based on MCU, which only needs to debug parameters through experimental processing, making it a common control algorithm in control systems.

Digital PID algorithms are generally divided into position PID and incremental PID. The incremental PID does not require accumulation; the control value of incremental PID is only related to the latest several deviation sampling values, and the impact of calculation errors of the control value is small. Moreover, the incremental PID yields the increment of the control value, which minimizes influence from mis-operations. Due to above advantages, incremental PID was selected for ROV motion control subsea.

Once force or torque required for each degree of freedom determined through PID algorithm, it is necessary to solve output of each actuator through some kind of thrust allocation algorithm [33, 34]. Generally, there are many ways of thrust allocation, including direct allocation method [35], pseudo inverse allocation method [36], optimization allocation method based on mathematical programming [37], and swarm intelligence optimization allocation method. In practical engineering applications, we employ the STM32F427 microcontroller to perform the control computations. This processor offers sufficient computational capability to execute both the Traversal method and the Moore–Penrose pseudo-inverse approach for thrust allocation. Given that thrust allocation for over-actuated underwater vehicles has been extensively studied and widely implemented in engineering practice, it is not considered a focal point or a key contribution of this paper. The motion control strategy in vertical plane of the developed ROV is relatively simple and does not involve complex thrust distribution strategies. The motion control in vertical plane, however, is an over-actuated system and the allocation processing must consider the actual characteristics of the ROV. The principles for thrust allocation in horizontal plane are as follows:

(1) Limited by output power of submersible battery, the total power consumption of the four horizontal thrusters shall be below four hundred watts; according to the thrust-power consumption curve, the total thrust of 4 horizontal shall not exceed six kilograms.

(2) To balance the output thrust of four horizontal thrusters, the maximum output thrust of each thruster should be limited by two kilograms.

(3) Priority is given to ensuring the output of rotational torque, i.e., prioritizing the ROV's heading control function.

(4) The traversal method is used to pick out the thrust allocation which has minimum sum of output thrust of four horizontal thrusters, that is good for overall power consumption of ROV.

(5) In case there is a faulty thruster, a fault-tolerant mechanism is activated to complete thrust allocation through the other three thrusters.

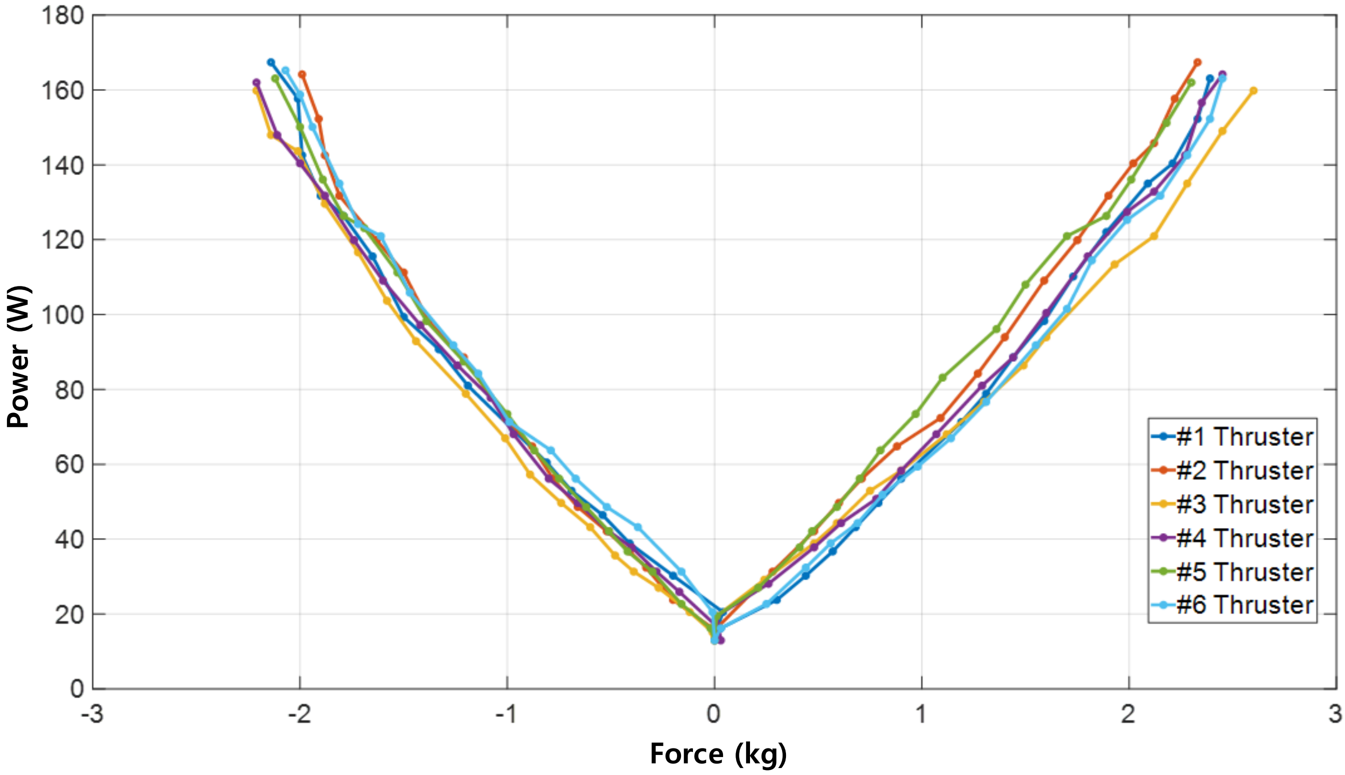

Fig. 12 Relationship Between Thrust and Power Consumption of Each Thruster

Figure 12 shows the relationship between the thrust and actual power consumption of six thrusters mounted on the ROV. It is obvious that all the curves of six thrusters are in good consistency. As presented in Table 6, the coefficients of determination (R^2) of the fitted curves are all close to 1.0, indicating that the relationship between thruster force and power consumption can be well approximated by a linear model.

Table 6 Statistical Table of Coefficient of Determination R2 for Fitted Lines of Thruster Thrust-Power Consumption

Thruster NO	R^2/Pos. Half-Axis	R^2/Neg. Half-Axis
#1	0.9884	0.9872
#2	0.9875	0.9743
#3	0.9924	0.9832
#4	0.9910	0.9870
#5	0.9895	0.9918
#6	0.9971	0.9922

5.2 Program design

As known from the previous text, the main control software is developed based on the microprocessor STM32F427, which runs Free-RTOS operating system. In addition to the conventional electrical control function and communication function, implementation of the motion control algorithm is the core of main control program.

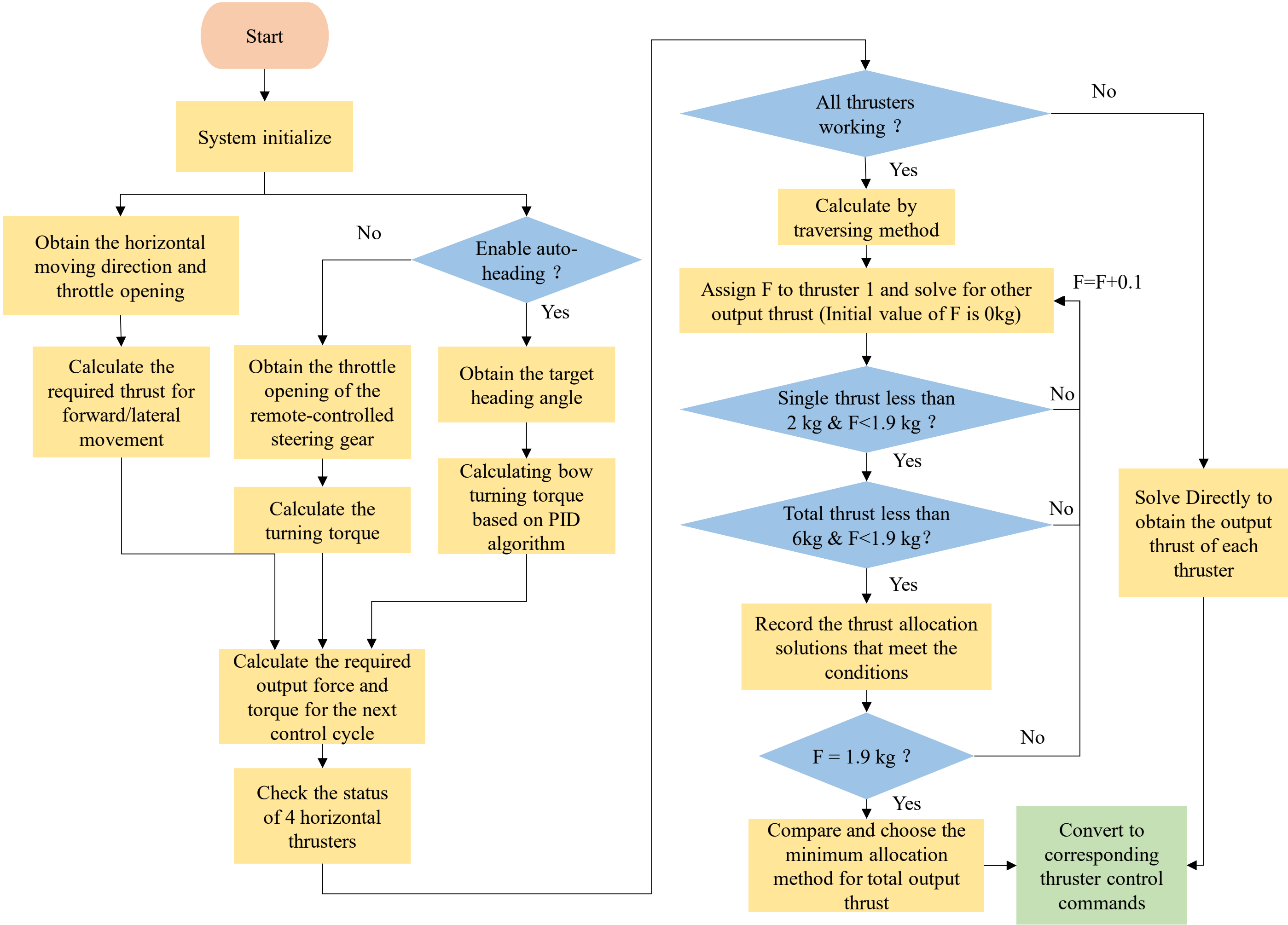

Fig. 13 Flowchart of Motion Control Algorithm in Horizontal Plane

As is shown in Figure 13, The motion control algorithm in horizontal plane is implemented by MCU. Once system initialized, whether the auto-heading function is enabled should be judged. If enabled, the required turning torque is calculated through the incremental PID; if not enabled, the required turning torque is parsed based on the heading throttle opening of remote monitoring system. Next, according to the moving direction and throttle opening in horizontal plane, the thrust requirements for bow direction and side direction of the vehicle are calculated. Based on above results, thrust allocation begins: firstly, make a judgement whether all 4 horizontal thrusters are working: only three thrusters works, the thrust allocation of any three thrusters can be directly calculated; the quantity of thrusters in under normal conditions is below three, thrust allocation cannot be implemented, and the ROV needs to be recovered and fixed; all four thrusters are working normally, the traversal method is used for thrust allocation. During traversal processing, a total of 20 calculations need to be completed. Assume that the initial thrust of NO. 1 thruster is 0, calculate the required thrust of other three thrusters. Only when sum of all thrusters' forces is less than 6 kg and thrust of each thruster is less than 2 kg can processor record this thrust allocation combination as a valid combination. After completing calculations 20 times, select the combination with the smallest total thrust among all valid combinations as the optimal combination. Finally, according to this combination, convert the force of each thruster to output opening, that is, the actual control command of the control board. One cycle done, the above procedure is executed repeatedly continuously to achieve motion control of the ROV in horizontal plane.

6. Experiment validation

During the development of the deep-sea micro-observation-class ROV, many tests were conducted in stages. Firstly, single test: tests of forward 4K camera, backward AHD camera, thrusters, motor driver boards, winch drive motor, power supply boards, optical fiber communication, and pressure test of every component, etc. Next, integration and debugging: ROV assembly, ROV attitude and buoyancy trimming underwater, basic control function, automatic motion control functions, observation capabilities underwater.

6.1 Assembly and land test

According to the design drawings, complete manufacture of each part, assemble of whole vehicle, including main frame, buoyancy materials, peripheral devices, and umbilical cable. ROV pictures during assembly processing is shown in Figure 14.

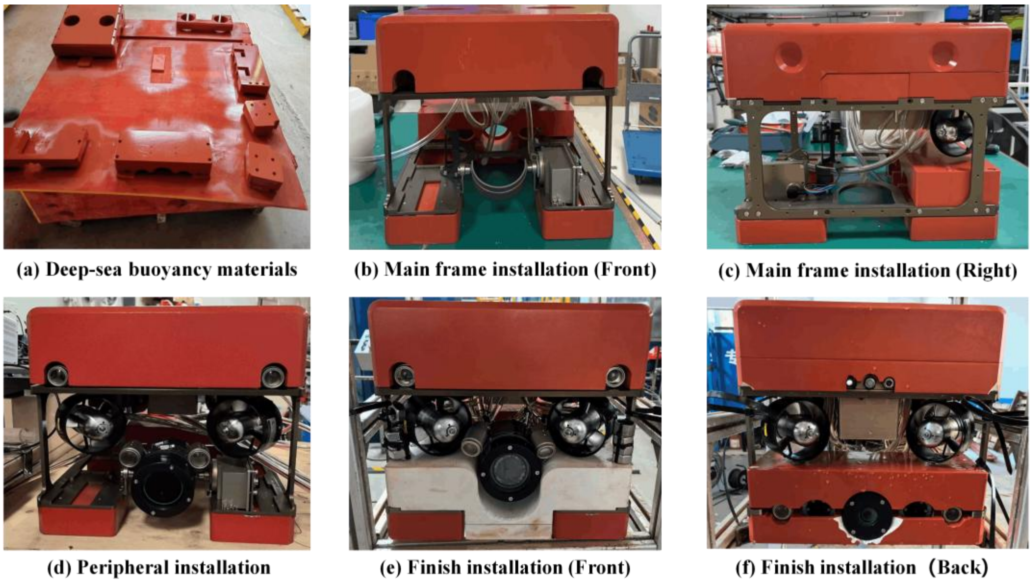

Fig. 14 ROV pictures during the assemble processing

In addition to the ROV assembly, docking station and winch have also been manufactured and assembled. Pictures of these three parts are shown in Figure 15.

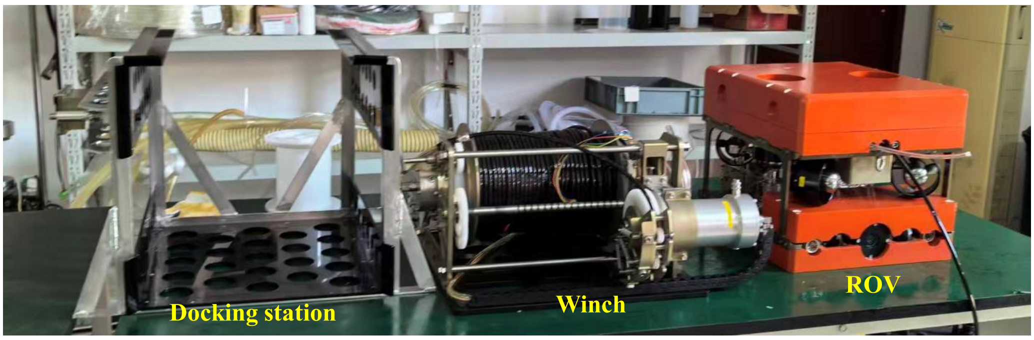

Fig. 15 Picture of each component of the ROV system

All assembly done, it is necessary to confirm the functions of each part to ensure that they meet the desired goal, laying a strong foundation for pool test and sea-trial.

6.2 Pool test

During stage of pool testing, firstly, weigh ROV weight underwater to ensure that the ROV has a slight buoyancy when completely submerged in water. Then, adjust attitude of the ROV underwater to ensure there is no obvious inclination when completely submerged. After completing the above two steps, ROV motion control function can start to be carried out, including remote manual control, auto-altitude and auto-heading control. This is the most important part of ROV testing which needs to adjust parameters of incremental PID to ensure stable and accurate motion function subsea. Finally, observation ability of the ROV will be tested, which will be conducted at night considering deep-sea dark environment. As shown in Figure 16, before pool test, the deployment work is completed and then motion control in horizontal plane and vertical plane are carried out. As shown in Figure 17, observation function while ROV moving was tested. After continuous testing and optimization, forward camera's imaging resolution can reach 4K level in reality.

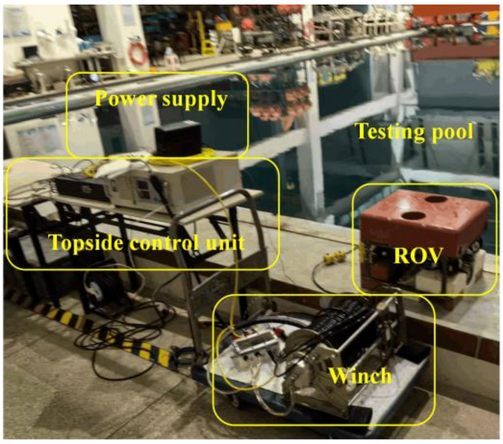

(a) Deployment of system pool testing

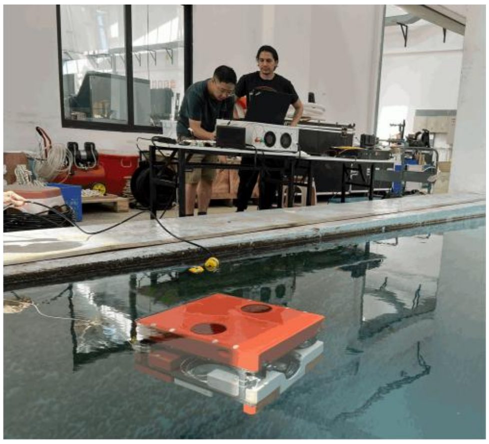

(b) Pool test operation

(c) Horizontal plane motion control test of ROV

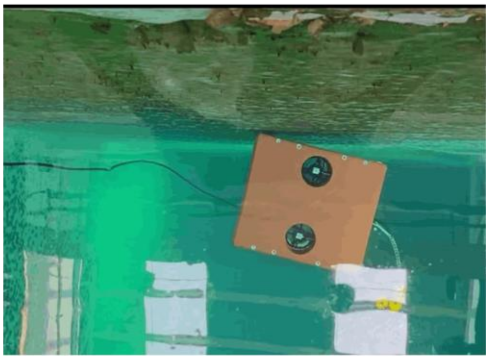

(d) Auto-altitude test of ROV

Fig. 16 Deployment and motion control test during pool test processing

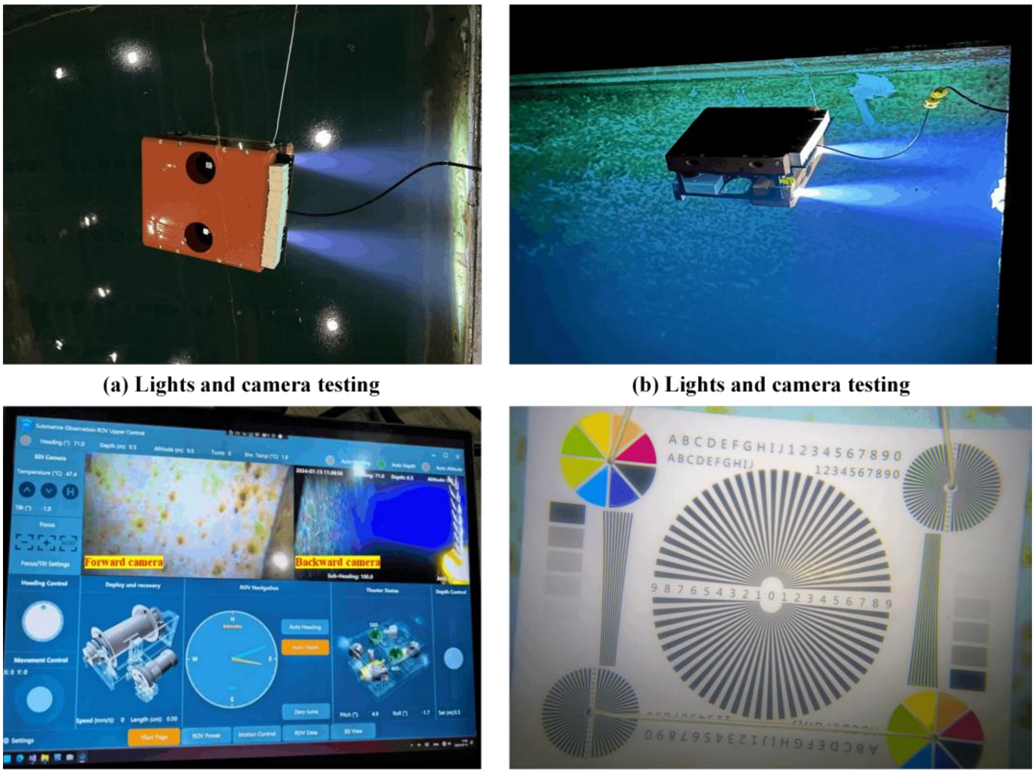

(a) Lights and camera testing (b) Lights and camera testing

(c) Main page of user interface (d) Image acquired by forward looking camera

Fig. 17 Observation capability test of ROV subsea

6.3 Sea-trial

Before sea trial, a pressure test of whole system was conducted with a test pressure of 57.5 MPa for 10 cycles. The ROV system (including ROV and winch unit) was mounted on a pressure testing fixture and deployed into a pressure test chamber tank as shown in Figure 18. The figure also shows the data records during the pressure testing processing, slowly rising from atmospheric pressure to 57.5 MPa, then holding pressure for 10 min, finally releasing the pressure to atmospheric pressure, that is one cycle.

After completion of the above verifications, the ROV system participated in the TS2-38-7 voyage segment of the R/V Tan Suo Er Hao which is organized by Institute of Deep-Sea Science and Engineering, Chinese Academy of Sciences. The whole system was mounted on HOV Shen Hai Yong Shi during dive SY713, in which the ROV system completed 2 h subsea tests in Haima Cold Seep area, with a maximum operating depth of 1387.5 m, and a maximum distance of 17 m from the HOV for observation operations.

It should be emphasized that, during the SY713 sea trials, the locking mechanism of the docking station shown in Figure 15 had not yet completed full functional validation. Consequently, the HOV Shen Hai Yong Shi carried only the ROV, without the dedicated docking station. During the sea trials, the HOV manipulators were employed as the primary alternative to the docking station. Specifically, the manipulators were used to accomplish the subsea deployment and recovery of the ROV, including launch from and recovery to the HOV. In detail, as illustrated in Figures 18(c) and 18(d), iron-sand ballast bags were attached to the ROV to provide additional negative buoyancy. Meanwhile, the manipulator was used to hold the handle located on the top of the ROV, ensuring that the vehicle remained securely positioned within the HOV sampling basket during both descent and ascent. After the HOV reached the destination with the ROV inside the sampling basket, the manipulator removed the ballast bags from the top of the ROV. Subsequently, the manipulator grasped the top handle to lift the ROV out of the basket and release it for operation. Upon completion of the mission, the ROV navigated to the front of the HOV sampling basket. One manipulator grasped the top handle to place the ROV back into the basket, while the other manipulator repositioned the ballast bags onto the top of the vehicle. In this manner, secure fixation, deployment, and recovery of the ROV from the HOV were successfully achieved.

Figure 18 shows the picture of the ROV system being integrated with HOV Shen Hai Yong Shi, deployed on the sampling basket of HOV, and finally diving to deep-sea seabed with the HOV. Figure 19 shows pilot operating inside HOV Shen Hai Yong Shi, seabed scenery of Haima Cold Seep area. By accident, pilot found it is very good to track ROV position through image sonar of HOV. Figure 20 displays pictures taken from inside submersible while ROV moving away from the HOV. Figure 21 shows the recording data of depth during ROV operation subsea which lasts more than 2 hours. And the PID gains for the depth control are K_p = 1800, K_i = 15, and K_d = 0.

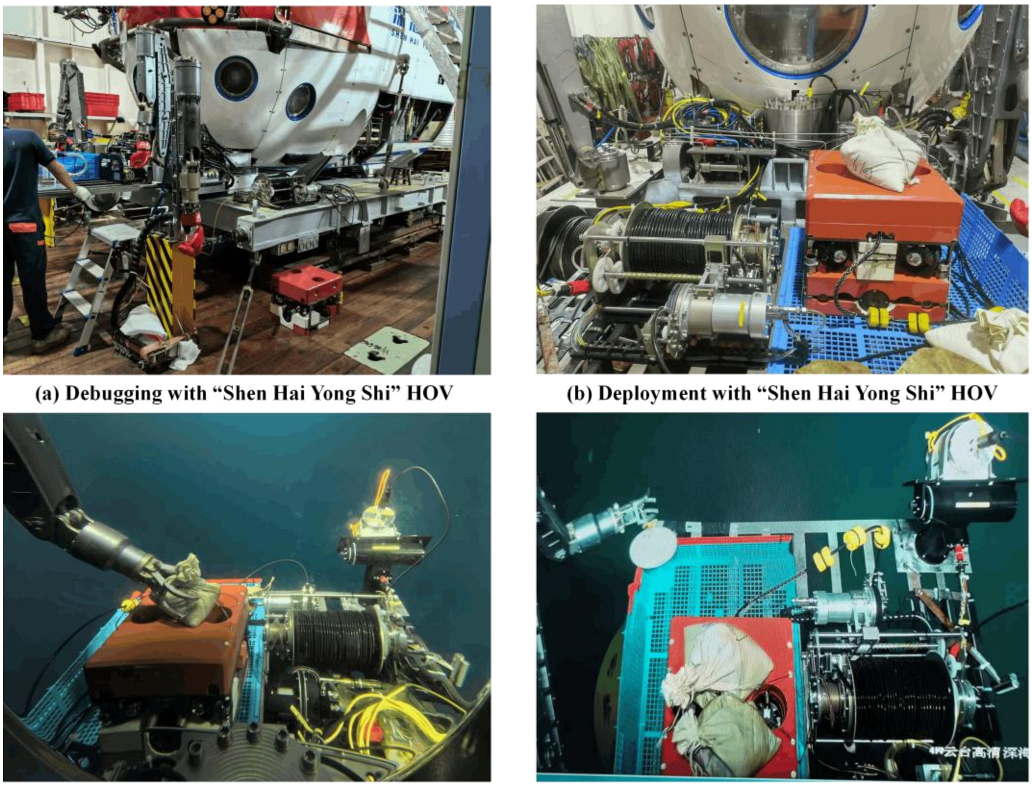

(a) Debugging with "Shen Hai Yong Shi" HOV (b) Deployment with "Shen Hai Yong Shi" HOV

(c) Diving with "Shen Hai Yong Shi" HOV (d) Deep-sea view through "Shen Hai Yong Shi" HOV

Fig. 18 ROV deployed on HOV *Shen Hai Yong Shi*, diving with HOV to deep sea

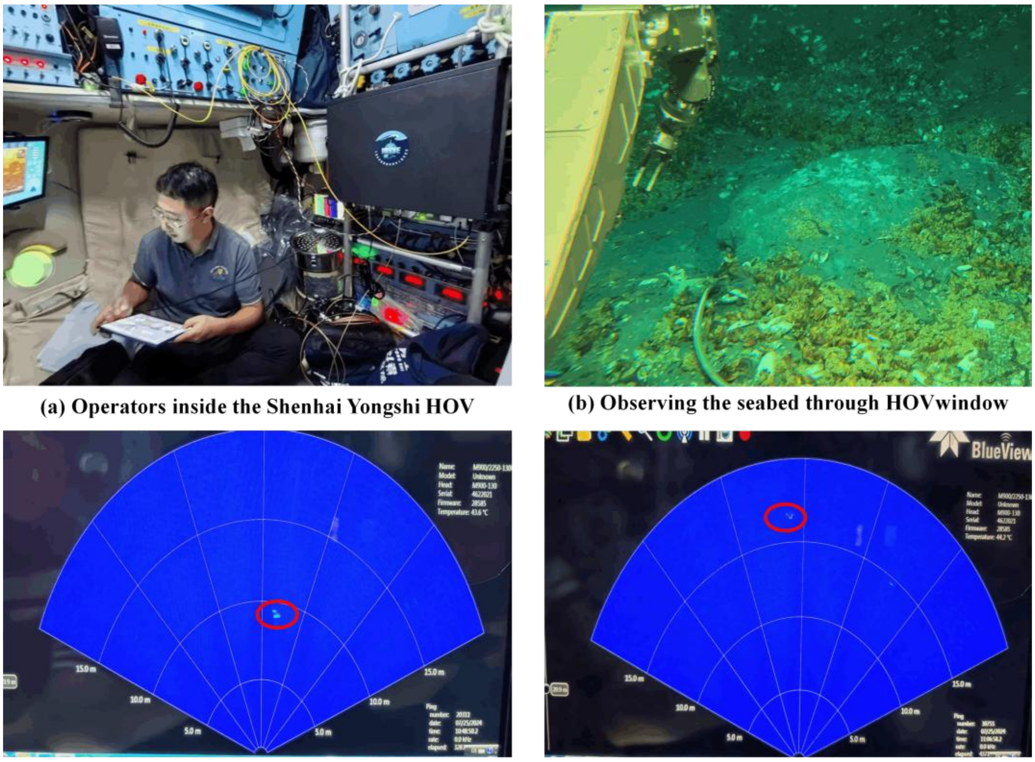

(a) Operators inside the Shenhai Yongshi HOV

(b) Observing the seabed through HOVwindow

(c) Observing ROV through HOV sonar

(d) Observing ROV through HOV sonar

Fig. 19 Operating the ROV inside HOV

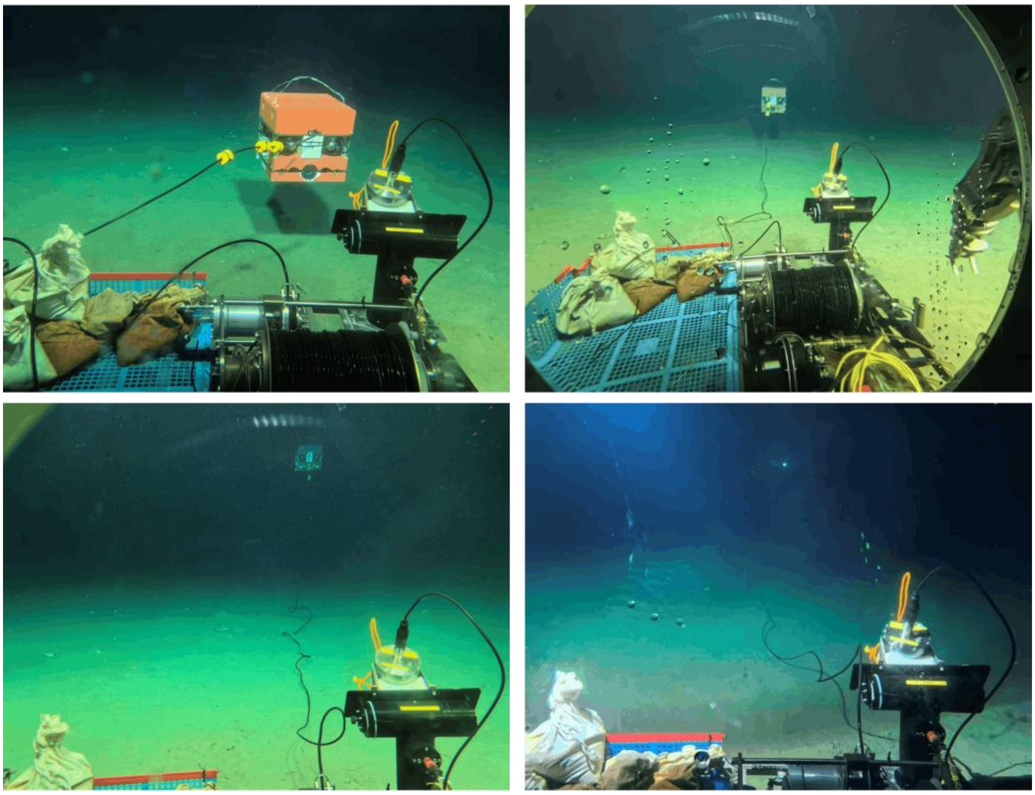

Fig. 20 Observing ROV moving away from HOV through the HOV window

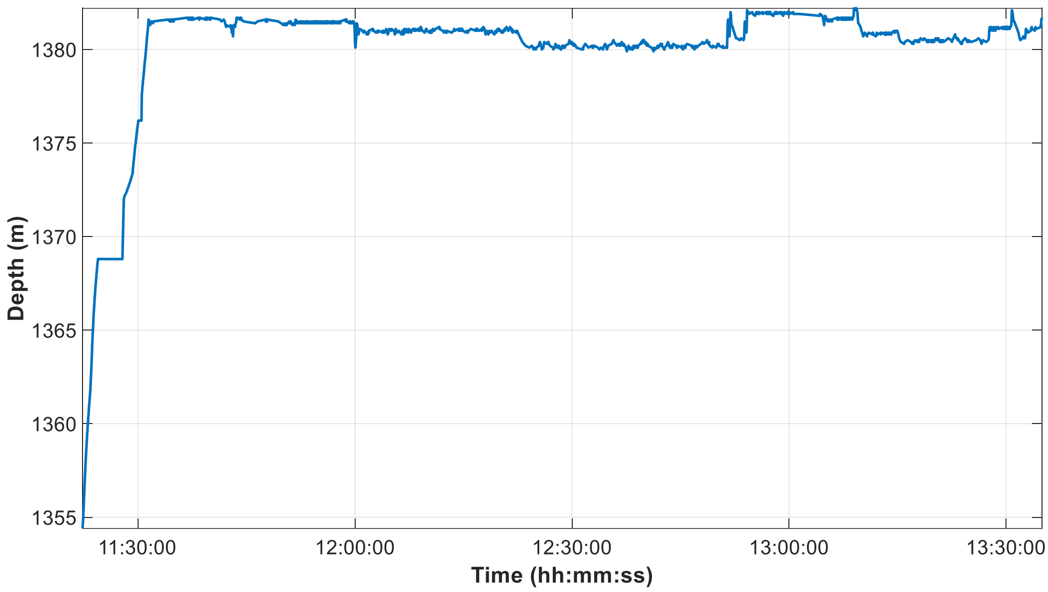

Fig. 21 Depth Data Over Time During Operation Subsea

During pool test and sea trial processing, a number of test data was obtained, as shown in Figures 21-24 respectively.

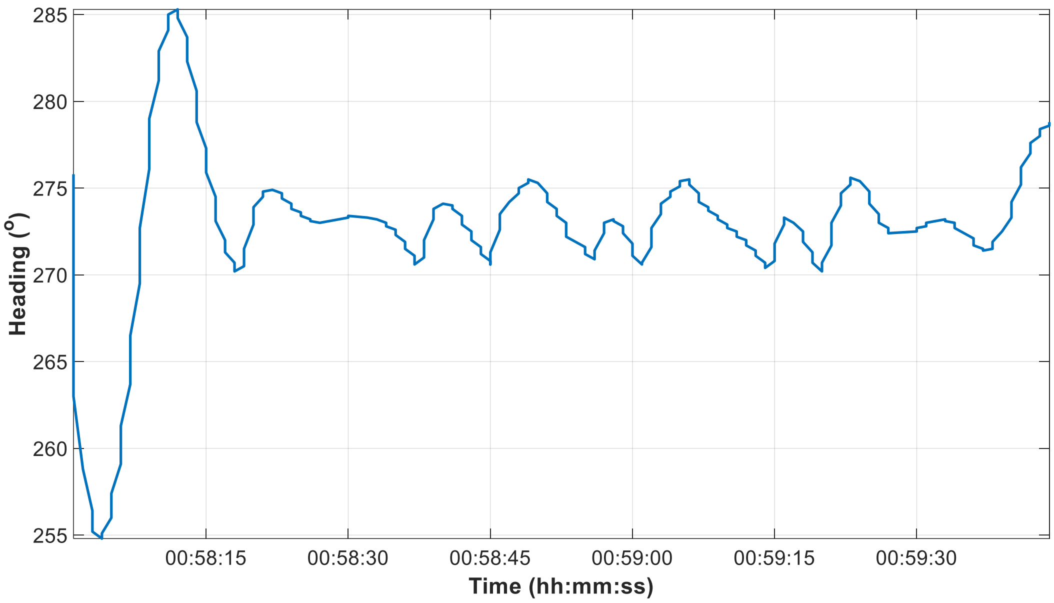

Fig. 22 Heading Over Time During Auto-heading (273°) Processing

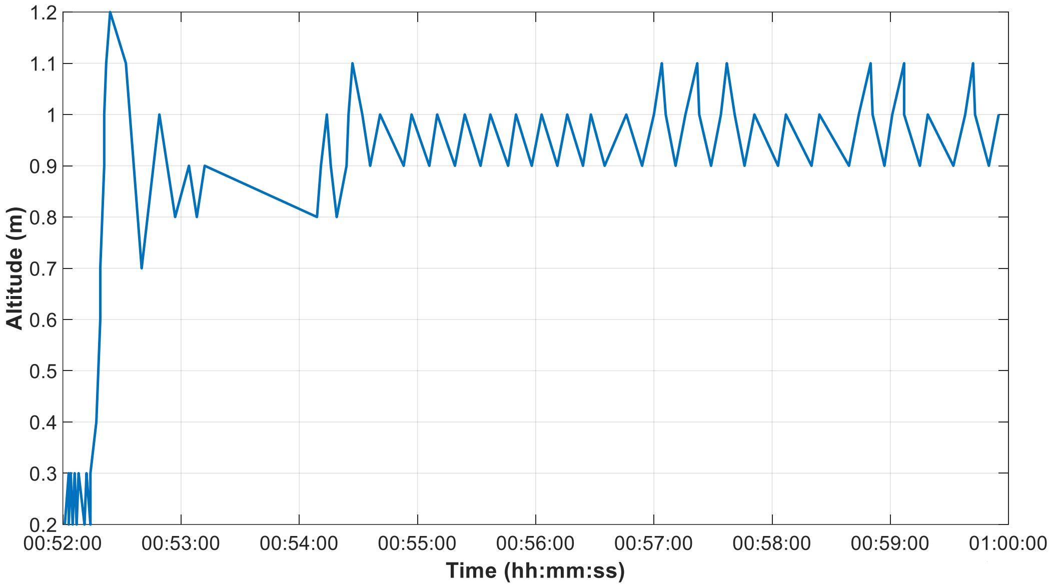

Fig. 23 Altitude From Seabed Over Time During Auto-Altitude (1 m) Processing

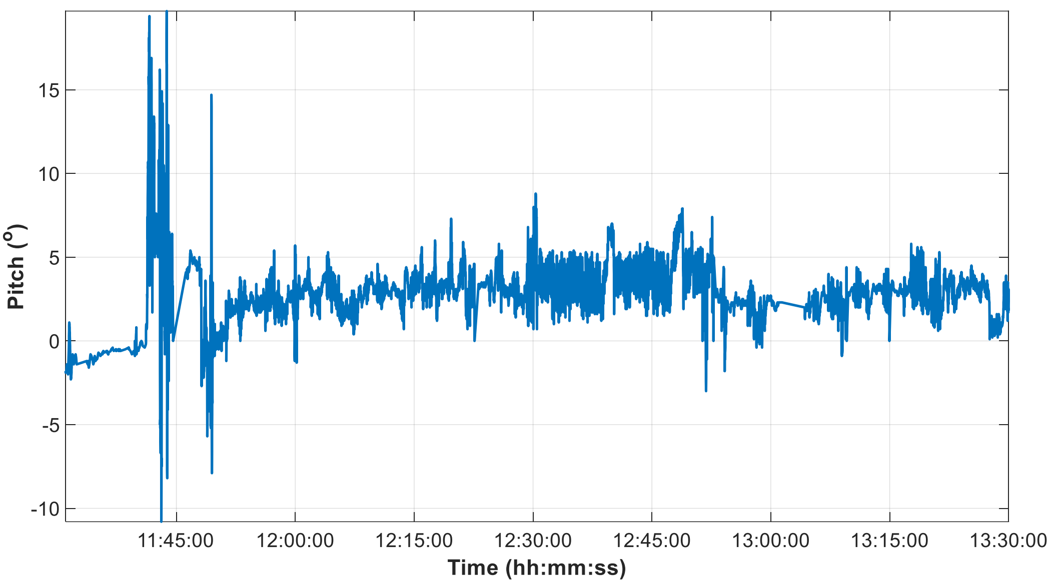

Fig. 24 Pitch Angle Over Time During Subsea Operation

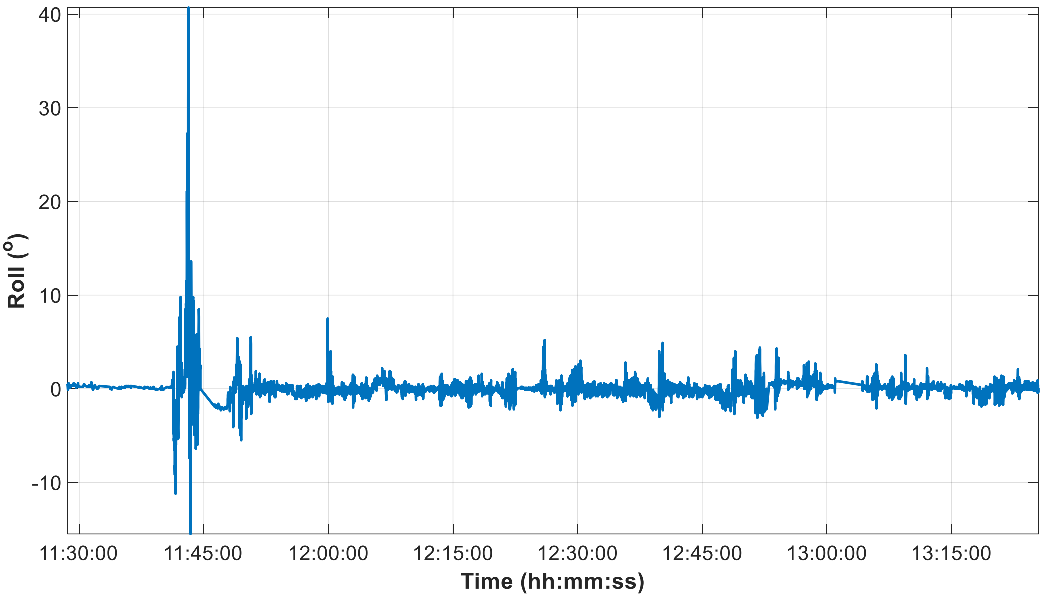

Fig. 25 Roll Angle Over Time During Subsea Operation

Figure 22 shows ROV heading angle changing over time during the automatic heading control. The PID control parameters for the ROV heading (yaw) regulation are set as Kp = 25, Ki = 0, and Kd = 0. The desired heading angle is 273°, and the actual heading angle is around 273° during steady-state phase. As shown in Table 7, the mean absolute error is 1.13°, the root mean square error is 1.40°, and the maximum absolute deviation is 3.20°. Figure 23 shows ROV altitude changing above the seabed over time during the automatic altitude control. The PID control parameters for the ROV heading (yaw) regulation are set as Kp = 1800, Ki = 15, and Kd = 0. The desired altitude of ROV above the seabed is 1m, and the actual altitude is around 1m during steady-state phase. As is shown in Table 7, the mean absolute error is 0.05 m, the root mean square error is 0.08 m, and the maximum absolute deviation is 0.20 m.

Table 7 Quantitative Steady-State Error Indicators of Automatic Heading & Altitude Control

Control Mode	Target Value	MAE	RMSE	Max. Abs. Dev.
Auto Heading (°)	273	1.13	1.40	3.20
Auto Altitude (m)	1	0.05	0.08	0.20

Figures 24 and 25 respectively show the pitch angle and roll angle of ROV subsea over time during its seabed operation. Due to ROV has not yet separated from sampling basket of the HOV in initial stage, ROV's roll angle is around 0° and pitch angle is around -2°, which is the same as HOV. When the ROV is separated from or recovery on the sampling basket, it is grabbed by manipulator from the ring on the top of the ROV, resulting in a relatively large range of angle change. During underwater operation of the ROV, the disturbance force exerted by the umbilical cable at the stern is generally small. However, due to constraints in the vehicle's structural configuration and control architecture, the ROV is not equipped with a closed-loop pitch control system, resulting in limited capability to suppress pitch disturbances. When external disturbances cause the pitch angle to deviate from its equilibrium position, the vehicle undergoes free oscillatory motion about the equilibrium attitude under the action of the hydrostatic restoring moment generated by buoyancy. The natural pitch period is an inherent dynamic characteristic of the ROV and is determined by the vehicle's mass moment of inertia, hydrodynamic added moment of inertia, and hydrostatic restoring stiffness. It is independent of the magnitude of the external excitation. As shown in Figure 24, the ROV exhibits a pitch angle of approximately 4°, oscillating within a range of about 1°–5° around the equilibrium attitude. In most periods, as shown in Figure 25, ROV's roll angle remains around 0°. In general, ROV's pitch angle and roll angle are relatively stable, and the overall attitude in water is stable. For the sake of sufficient design and testing in the early stage, ROV got a neutral state without turning any thrusters when at deep sea.

7. Conclusion

This paper presents the architecture and configuration design of micro-observation-class ROV deployed on the HOV Shen Hai Yong Shi, along with the application results from deep-sea sea trials. Particularly, the design and implementation of the ROV's mechanical system, electrical system and motion control system are analyzed. Compared with the existing HOV-borne ROVs, the proposed ROV adopts a communication and power supply method using the HOV's optoelectronic composite umbilical cable. This design provides sufficient weight and space margins for the arrangement of thrusters and detection sensors, further enhancing the ROV's lightweight construction, motion flexibility and diversity of detection payloads.

Retrospectively, considerable efforts have been devoted into the miniaturization and lightweight design of the peripheral components, including compact deep-sea thrusters, a micro 4K imaging system, an ROV maneuvering system and LED lighting modules, for the development of the HOV-borne micro-observation-class ROV. The preliminary deep-sea application trials indicate that the ROV's observation and manipulation capabilities meet the fundamental requirements for deep-sea operations. However, its reliability and detection performance require further improvement. Therefore, the following enhancement measures are proposed for future development and system upgrades.

(1) Regarding system integration, the junction box is currently located in the midsection of the ROV, housing several stacked control circuit boards. This configuration is unfavorable for assembly, disassembly and maintenance. Future designs will focus on improving system modularity and maintenance.

(2) For the propulsion system, deep-sea thrusters with a rated voltage compatible with the HOV power system will be adopted. In this configuration, the power system can drive the thrusters directly without the need for DC–DC conversion, thereby simplifying the power distribution architecture and the efficiency and reliability of the enhancing system.

(3) With respect to underwater testing, further systematic tests on the ROV are required to continuously identify design deficiencies and optimise system performance. Only through iterative testing and improvement can the intended design goals be fully achieved, enabling the ROV to enhance the exploration capability of the HOV over complex seafloor terrain.

(4) To overcome the limitation in attitude control, vertical thrusters can be integrated into the propulsion system to provide closed-loop control of the pitch and roll degrees of freedom. This configuration can substantially enhance the ROV's attitude stabilization capability, resulting in improved motion performance.

ACKNOWLEDGMENTS

The authors gratefully acknowledge the effort made by the team of IDSSE, CAS, including Deep-sea Resource Development group, Deep-Sea Submersible Technology group and sea trial support from R/V Tan Suo Er Hao. Useful suggestions were given by Ming Chen, June Liu, Chao Xie of IDSSE also acknowledged.

FUNDING

This research was supported by National Key R&D Program of China (No. 2024YFB4710802), National Natural Science Foundation of China (No. 52301372 and No. 52131101), National Key Research and Development Program of China - Intergovernmental International Scientific and Technological Innovation and Cooperation Program (No. 2023YFE0115400), National Science and Technology Major Project of China (No. 2025ZD1403700), Interdiciplinary Research Program of HUST (No. 2024JCYJ030 and No. 2025JCYJ018), and Sub project under the Key Deployment Project of the Chinese Academy of Sciences (NO. KGFZD-145-22-06-03-01).

REFERENCES

[1] Hein, J. R., Koschinsky, A., Kuhn, T., 2020. Deep-ocean polymetallic nodules as a resource for critical materials. *Nature Reviews Earth & Environment*, 1(3), 158-169. https://doi.org/10.1038/s43017-020-0027-0

[2] Levin, L. A., Bett, B. J., Gates, A. R., Heimbach, P., Howe, B. M., Janssen, F., Weller, R. A., 2019. Global observing needs in the deep ocean. *Frontiers in Marine Science*, 6, 241. https://doi.org/10.3389/fmars.2019.00241

[3] Cui, W., Shao, X., 2025. Current progress and future development trends of deep-sea exploration technology. *Science & Technology Review*, 43(12), 38-54.

[4] Zhang, J., Xiang, X., Zhang, Q., Tao, B., 2024, Electromagnetic localization and tracking control of underactuated autonomous underwater vehicle for subsea cable detection. *IEEE Transactions on Vehicular Technology*, 73(12), 18283-18293. https://doi.org/10.1109/TVT.2024.3442299

[5] Zhang J, Wang A, Liu Y, et al. Simultaneous electromagnetic localization, guidance and control of underactuated AUV for autonomous subsea cable inspection. *Journal of Ocean Engineering and Science*, 2026. https://doi.org/10.1016/j.joes.2026.03.007

[6] Zhang, J., Xiang, X., Li, W., Zhang, Q., 2023. Adaptive neural control of flight-style AUV for subsea cable tracking under electromagnetic localization guidance. *IEEE/ASME Transactions on Mechatronics*, 28(5), 2976-2987. https://doi.org/10.1109/TMECH.2023.3256707

[7] Yang, B., Liu, Y., Liao, J., 2021. Manned submersibles—deep-sea scientific research and exploitation of marine resources. *Bulletin of Chinese Academy of Sciences*, 36(5), 622-631.

[8] Liu, B., Ding, Z., Shi, X., Yu, K., Li, D., Li, B., 2015. Progress of the application and research of manned submersibles used in deep sea scientific investigations. *Acta Oceanologica Sinica*, 37(10), 1-10.

[9] Peng, X., Zhang, W., Schnabel, K., Leduc, D., Xu, H., Zhang, H., Rowden, A., 2023. Unveiling the mysteries of the Kermadec Trench. *The Innovation*, *4*(1), 100367. https://doi.org/10.1016/j.xinn.2022.100367

[10] Shi, L., Guo, S., Pan, S., He, Y., Guo, P., 2013. A multifunctional underwater microrobot for mother-son underwater robot system. *IEEE International Conference on Robotics and Biomimetics*, 12-14 December, Shenzhen, China. https://doi.org/10.1109/ROBIO.2013.6739595

[11] Yang, L., Zhao, S., Wang, X., Shen, P., Zhang, T., 2022. Deep-sea underwater cooperative operation of manned/unmanned submersible and surface vehicles for different application scenarios. *Journal of Marine Science and Engineering*, 10(7), 909. https://doi.org/10.3390/jmse10070909

[12] Roddy Jr, R. F., Lange, W. N., Nesmeyanov, E. V., Woytowich, R. L., 2022. Evolution of Evolution of Titanic Breakup Theories and the Accepted SNAME MFC Theory. *SNAME Maritime Convention*, 27–29 September, Houston, Texas, United States. https://doi.org/10.5957/SMC-2022-009

[13] Cao, J., Xu, W., Hu, Z., Jiang, L., Yang, Q., 2021. Research on mother-child cooperative technology of manned/unmanned underwater vehicle. *Proceedings of the 4th Underwater Unmanned System Technology Summit Forum*, 4 December, Xi'an, China.

[14] Li, Y., Li, S., Zhang, A., 2016. Research status of autonomous/remote controlled underwater vehicle. *Mechanical Management and Development*. 8, 217–221.

[15] Purzycki, M., Komorowska, A., Ilnicka, A., Papież, J., Szymańska, E., 2022. From ROVs to AUVs–Optimization and Analysis of Underwater Vehicles Design. *2022 45th Jubilee International Convention on Information, Communication and Electronic Technology*, 23-27 May, Opatija, Croatia. https://doi.org/10.23919/MIPRO55190.2022.9803712

[16] Sun, S., Luo, W., 2025. Multi-disciplinary optimization of underwater vehicles based on a dynamic proxy model. *Brodogradnja*, 76(3), 76306. https://doi.org/10.21278/brod76306

[17] Jiang, L., Long, R., Wang, Y., Su, X., 2024. Application of system thinking in the design of manned submersible. *Ship Science and Technology*, 46(6), 1-6.

[18] Said, M. F. M., Roslan, I. S., Bakar, S. A., 2015. Conceptual design of remotely operated underwater vehicle. *Journal of Transport System Engineering*, 2(1), 15-19.

[19] Wang, Y. L., Lu, C. Y., 2012. Design and parameter estimation of a remotely operated underwater vehicle. *Journal of Marine Engineering & Technology*, 11(2), 39-48. https://doi.org/10.1080/20464177.2012.11020265

[20] Wang, Z., Xiang, X., Xiong, X., Yang, S., 2025. Position-based acoustic visual servo control for docking of autonomous underwater vehicle using deep reinforcement learning. *Robotics and Autonomous Systems*, 186, 104914. https://doi.org/10.1016/j.robot.2024.104914

[21] Liu, J., Wu, S., Yue, X., Yue, Q., 2024. Hydrodynamic shape optimization of an autonomous and remotely-operated vehicle via a multi-surrogate model. *Brodogradnja*, 75(3), 75301. https://doi.org/10.21278/brod75301

[22] Chen M, Liu Y, Zhu D, et al. Parameter identification of an open-frame underwater vehicle based on numerical simulation and quantum particle swarm optimization. *Intelligence & Robotics*, 2024, 4(2): 216-229. https://doi.org/10.20517/ir.2024.14

[23] Zeng T, Zhu D, Gu C, et al. An effective fault-tolerant control with slime mold algorithm for unmanned underwater vehicle. *Intelligence & Robotics*, 2025, 5(2): 276-291. https://doi.org/10.20517/ir.2025.14

[24] Sutrisno, I., Widiarti, Y., Rahmat, M. B., 2024. The Development of ROV (Remotely Operated Vehicle) by Applying PID (Proportional Integral Derivative) for Monitoring and Preservation of Coral Reefs at Pasir Putih Beach Situbondo. *Bulletin of Community Engagement*, 4(3), 583-590. https://doi.org/10.51278/bce.v4i3.1592

[25] Ren, F., Hu, Q., 2023. ROV sliding mode controller design and simulation. *Processes*, 11(8), 2359. https://doi.org/10.3390/pr11082359

[26] Einarsson, E. M., Lipenitis, A., 2020. Model Predictive Control for the BlueROV2. *Master Thesis,* Aalborg University, Fredrik Bajers Vej, Aalborg East, Denmark.

[27] Aras, M. S. M., Abdullah, S. S., Azis, F. A., 2015. Review on auto-depth control system for an unmanned underwater remotely operated vehicle (ROV) using intelligent controller. *Journal of Telecommunication, Electronic and Computer Engineering*, *7*(1), 47-55.

[28] Neira, J., Sequeiros, C., Huamani, R., Machaca, E., Fonseca, P., Nina, W., 2021. Review on unmanned underwater robotics, structure designs, materials, sensors, actuators, and navigation control. *Journal of Robotics*, *2021*(1), 5542920. https://doi.org/10.1155/2021/5542920

[29] Guan, W., Xi, Z., Cui, Z., Zhang, X., 2025. Adaptive trajectory controller design for unmanned surface vehicles based on SAC-PID. *Brodogradnja*, 76(2), 76206. https://doi.org/10.21278/brod76206

[30] Evers, B., Manley, J., 2007. A vehicle for science and exploration: Bringing offshore industry advances and experience to the oceanographic community. In *OCEANS 2007*, 29 September-4 October, Vancouver, Canada. https://doi.org/10.1109/OCEANS.2007.4449314

[31] Zhang, Y., Zhang, J., Guo, Z., Zhang, L., Shang, Y., 2025. An adaptive NMPC for ROVs trajectory tracking with environmental disturbances and model uncertainties. *Brodogradnja*, 76(1), 76106. https://doi.org/10.21278/brod76106

[32] Cao, H., Zhang Q., Tang S., 2021. Current status and key technologies of Remotely Operated Vehicles in international submarine rescue and deep-sea salvage. *Ship Science and Technology*, 43(12), 16-20. https://doi.org/10.34133/cbsystems.0089

[33] Huang, H., Zhang, G. C., Yang, Y., Xu, J. Y., Li, J. Y., Wan, L., 2016. Advances in Swarm Intelligence. *Springer*, Dordrecht, Netherlands.

[34] Fossen, T. I., Johansen, T. A., Perez, T., 2009. Underwater vehicles. *IntechOpen*, London, UNITED KINGDOM.

[35] Ren, F., Guo, X., Deng, X., Wang, B., Wang, Z., 2025. The Design of a New Type of Remotely Operated Vehicle System and the Realization of a Thrust Distribution Method. *Applied Sciences*, *15*(8), 4199. https://doi.org/10.3390/app15084199

[36] Kajanus, R., 2014. Optimal recursive thrust allocation applied for rov Minerva. *Master Thesis*, Norwegian University of Science and Technology, Høgskoleringen, Trondheim, Norwegian.

[37] Zhao, B., Sun, X., Xia, G., 2019. Improved Generalized-Inverse-Based Thrust Allocation for Dynamic Positioning Vessels with Rotatable Thrusters and Force Constraint. *2019 Chinese Automation Congress*, 22-24 November, Hangzhou, China. https://doi.org/10.1109/CAC48633.2019.8996299